The influence of submerged coastal structures on nearshore flows and wave runup

da Silva, Renan F.; Hansen, Jeff E.; Rijnsdorp, Dirk P.; Lowe, Ryan J.; Buckley, Mark L.

DOI
10.1016/j.coastaleng.2022.104194

Publication date
2022

Document Version
Final published version

Published in
Coastal Engineering

Coastal Engineering 177 (2022) 104194

Contents lists available at ScienceDirect

Coastal Engineering

journal homepage: www.elsevier.com/locate/coastaleng

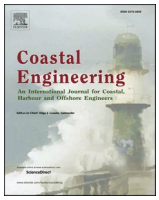

The influence of submerged coastal structures on nearshore flows and wave runup

Renan F. da Silva [a,b,c,d,*], Jeff E. Hansen [a,b,c,e], Dirk P. Rijnsdorp [f], Ryan J. Lowe [a,b,c,d,e], Mark L. Buckley [g]

[a] School of Earth Sciences, The University of Western Australia, Crawley, WA, 6009, Australia
[b] UWA Oceans Institute, The University of Western Australia, Crawley, WA, 6009, Australia
[c] Marine Energy Research Australia, The University of Western Australia, Crawley, WA, 6009, Australia
[d] ARC Centre of Excellence for Coral Reef Studies, The University of Western Australia, Crawley, WA, 6009, Australia
[e] Oceans Graduate School, The University of Western Australia, Crawley, WA, 6009, Australia
[f] Environmental Fluid Mechanics Section, Faculty of Civil Engineering and Geosciences, Delft University of Technology, P.O. Box 5048, 2600 GA, Delft, the Netherlands
[g] U.S. Geological Survey, St. Petersburg Coastal and Marine Science Center, St. Petersburg, FL, USA

ARTICLE INFO

Keywords:
Submerged coastal structures
Submerged breakwaters
Reefs
Wave-driven flows
Wave runup
Phase-resolved wave modelling

ABSTRACT

Engineered and natural submerged coastal structures (e.g., submerged breakwaters and reefs) modify incident wave fields and thus can alter hydrodynamic processes adjacent to coastlines. Although submerged structures are generally assumed to promote beach protection by dissipating waves offshore and creating sheltered conditions in their lee, their interaction with waves can result in mean wave-driven circulation patterns that may either promote shoreline accretion or erosion. Here, we analyse the mean flow patterns and shoreline water levels (wave runup) in the lee of idealised impermeable submerged structures with a phase-resolved nonhydrostatic numerical model. Waves propagating over submerged structures can drive either a 2-cell mean (wave-averaged) circulation, which is characterised by diverging flows behind the structure and at the shoreline, or 4-cell circulation, with converging flows at the shoreline and diverging flows in the immediate lee of the structure. The numerical results show that the mode of circulation can be predicted with a set of relationships depending on the incoming wave heights, the structure crest level, and distance to the shoreline (or structure depth). Qualitative agreement between the mean flow and proxies for the sediment transport using an energetics approach suggest that the mean flow can be a robust proxy for inferring sediment transport patterns. For the cases considered, the submerged structures had a minimal influence on shoreline wave setup and wave runup despite the wave energy dissipation by the structures due to alongshore wave energy fluxes in the lee. Consequently, these results suggest that the coastal protection provided by the range of impermeable submerged structures we modelled is primarily due to their capacity to promote beach accretion.

1. Introduction

Submerged structures are commonly found in proximity to coastlines worldwide, which can include a variety of engineered and natural structures. A well-known example of these structures are submerged breakwaters (e.g., Dean et al., 1997), which are designed to attenuate waves in their lee while being less aesthetically intrusive than emergent structures. Other examples of engineered structures include artificial surfing reefs (e.g., Black and Mead, 2001) and bottom-mounted wave energy converters (e.g., Ryan et al., 2015). Natural structures include barred beaches (e.g., Orzech et al., 2011) and both rocky (e.g., Segura et al., 2018) and coral reefs (e.g., Lowe et al., 2009).

In the nearshore zone, mean (wave-averaged) currents and water levels (setup and setdown) can develop in response to changes to wave fields through interactions with submerged structures. As waves propagate over shallow structures, they typically shoal and then break, thus creating sheltered wave conditions in their lee. The radiation stress gradients resulting from wave breaking generate mean water level (i.e., wave setup) differences in the lee of the structure and the net effect of radiation stress and setup gradients can drive mean currents (e.g., Haller

* Corresponding author. School of Earth Sciences, The University of Western Australia, Crawley, WA, 6009, Australia.
E-mail addresses: renan.silva@uwa.edu.au (R.F. da Silva), jeff.hansen@uwa.edu.au (J.E. Hansen), d.p.rijnsdorp@tudelft.nl (D.P. Rijnsdorp), ryan.lowe@uwa.edu.au (R.J. Lowe), mbuckley@usgs.gov (M.L. Buckley).

https://doi.org/10.1016/j.coastaleng.2022.104194
Received 1 February 2022; Received in revised form 6 June 2022; Accepted 30 July 2022
Available online 16 August 2022
0378-3839/

et al., 2002). These currents may affect sediment transport and ultimately result in shoreline changes (i.e., accretion or erosion, Ranasinghe et al., 2010, 2006). At the shoreline, mean wave setup and unsteady swash oscillations, which together determine the vertical elevation at the maximum landward excursion of water (i.e., wave runup), can also be reduced as a result of the attenuation of the waves caused by the structures (e.g., Hur et al., 2012).

Over the past few decades, submerged structures have attracted considerable research attention. A meta-analysis of the literature that described the shoreline response to constructed submerged breakwaters and artificial reefs found that 60% of them led to erosion in their lee (Ranasinghe and Turner, 2006) rather than the anticipated coastal protection, which indicates a limited understanding of their impacts on coastal processes. Most research to date on submerged breakwaters has focused on quantifying wave transmission (d'Angremond et al., 1997; Liang et al., 2015; Lorenzoni et al., 2012; Marin and Savov, 2017; van der Meer et al., 2005), which is expressed as a ratio between the transmitted and incident wave heights (usually obtained through 2D wave flume experiments). Wave flumes have also been used to measure the 2DV (vertical) velocities (Mohsin et al., 2011; Rathnayaka and Tajima, 2020) and to study the shoreline response (Lorenzoni et al., 2012) in the lee of submerged breakwaters. However, alongshore flow features cannot be accounted for in 2DV flume studies, such as wave diffraction/refraction and the presence of alongshore mean currents. These effects can influence the nearshore wave transformation, setup and swash hydrodynamics, and shoreline response, which motivates the need for more detailed investigation.

Due to the lack of detailed observations of hydrodynamics behind submerged structures (i.e., in laboratory wave basins and field studies), to date most investigations have relied on numerical modelling to evaluate the impact of submerged structures on nearshore hydrodynamics. Ranasinghe et al. (2010, 2006) evaluated the circulation pattern in the lee of impermeable submerged structures and found that wave breaking over submerged structures can drive a 2-cell circulation (Fig. 1a), with diverging flow in their lee, or a 4-cell circulation (Fig. 1b), also with divergence in their immediate lee but with converging currents at the shoreline. Hydrodynamic and morphodynamic modelling by Ranasinghe et al. (2006) indicated that these 2- and 4- cell circulation patterns can be linked with erosive and accretive shorelines, respectively. Relationships depending on wave and structure parameters to predict the mode of circulation as a proxy for shoreline response have also been proposed (Ranasinghe et al., 2010; van Der Baan, 2013; Villani et al., 2012).

In this study, we explore the detailed hydrodynamics in the lee of submerged structures for a wide range of wave conditions and structure geometries using phase-resolved modelling. The use of a phase-resolved wave-flow model allows us to account for the nonlinear intrawave motions in the description of the mean circulation patterns, which have not been previously resolved by existing studies. As will be shown, waves propagating over submerged structures undergo intense transformation; for instance, they may rapidly break, dissipate energy and create infragravity waves (i.e., waves with frequencies typically less than half the peak frequency, Longuet-Higgins and Stewart, 1962; Symonds et al., 1982). These nonlinear processes are expected to be important and need to be considered for a rigorous description of the hydrodynamics in the vicinity of submerged structures. Furthermore, with the intrawave hydrodynamics we can assess the hydrodynamic drivers of sediment transport as a function of time-varying bottom shear stresses and velocities (over both wave and wave-averaged time scales), and arguably achieve improved description of potential shoreline changes. Existing studies have either relied on mean circulation patterns as a proxy for shoreline response (Ranasinghe et al., 2010) or estimated shoreline changes with coupled circulation models (Ranasinghe et al., 2006; van Der Baan, 2013), which only resolve the mean (phase-averaged) currents, with the wave contribution to sediment transport being generally parameterised using linear wave theory. However, sediment suspension and transport is also dependent on wave orbital motions, generally assumed as proportional to the skewness of waves, and from the correlation between mean currents and waves, which depend on the intrawave hydrodynamics (Traykovski et al., 1999). In reef environments, several studies have demonstrated that the nonlinear intrawave hydrodynamics can largely influence or dominate bottom shear stresses (Cuttler et al., 2019; Rijnsdorp et al., 2021) and bedload sediment transport (Pomeroy et al., 2017), which ultimately will influence shoreline changes. Moreover, with the use of a phase-resolved model, we can directly resolve the full range of water motions that interact with shorelines, and by comparing cases with and without the presence of submerged structures, establish their effectiveness in affecting runup and protecting shorelines. Although several studies have established the role of coral reefs in reducing shoreline water levels (e.g., Buckley et al., 2018; Pearson et al., 2017; Quataert et al., 2015; Reguero et al., 2019), the influence of submerged structures with limited crest width (of order 10 m for typical breakwaters) on the mitigation of wave runup remains an open question (Hur et al., 2012; Irtem et al., 2011), which we address with our study.

In this study, we first characterise the circulation for representative cases resulting from the interaction between waves with submerged structures (Section 3.1). We also show how changes to the wave and

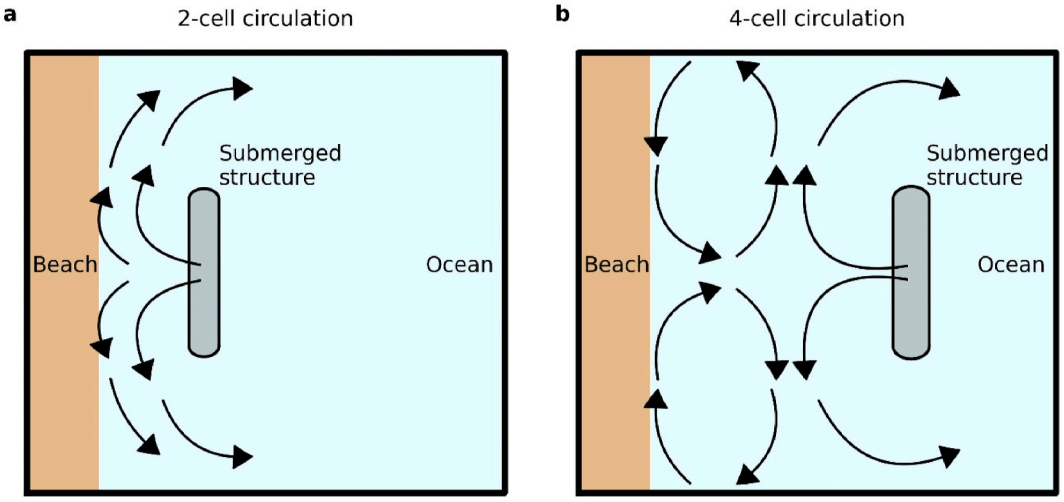

Fig. 1. Diagram of (**a**) 2-cell circulation (2CC) and (**b**) 4-cell circulation (4CC) patterns that can result from waves interacting with submerged structures. Arrows indicate mean (wave-averaged) flow patterns.

structure parameters influence the mean flow fields (Section 3.2), and with these findings propose a set of predictive relationships to characterise the flow patterns for each case (Section 3.3). Next, we assess the influence of submerged structures on shoreline water levels in their lee (Section 4). Then we evaluate the bottom shear stress patterns and proxies for sediment transport in the vicinity of submerged structures (Section 5). Finally, we discuss how submerged structures can influence the morphodynamics and wave runup and promote coastal protection (Section 6).

2. Methodology

2.1. Wave-flow numerical model

We applied the SWASH model version 6.01 (Zijlema et al., 2011; Zijlema and Stelling, 2005, 2008) to study the wave-driven flows and water levels in the lee of a single shore-parallel impermeable submerged structure. SWASH is a multilevel nonhydrostatic phase-resolving wave-flow model that solves the Reynolds-Averaged Navier-Stokes (RANS) equations and can thus simulate the nonlinear wave dynamics and generation of wave-induced currents in the nearshore zone (Rijnsdorp et al., 2017, 2021; Zhang et al., 2018). SWASH intrinsically accounts for the range of hydrodynamics processes that arise from wave transformation in the nearshore (e.g., nonlinear wave shape, energy transfers, diffraction, swash hydrodynamics, etc.) that are either absent or parameterised by phase-averaged numerical models. While nonhydrostatic models such as SWASH only provide a single-value representation of the free surface and hence cannot resolve wave overturning, SWASH has been shown to accurately represent the bulk dissipation associated with wave breaking (Smit et al., 2013). SWASH has been previously validated for barred beaches with rip channels (da Silva et al., 2021; Villani et al., 2012), whose bathymetries and associated flow patterns are conceptually similar to submerged structures (Ranasinghe et al., 2006). Several studies have also successfully used SWASH or other

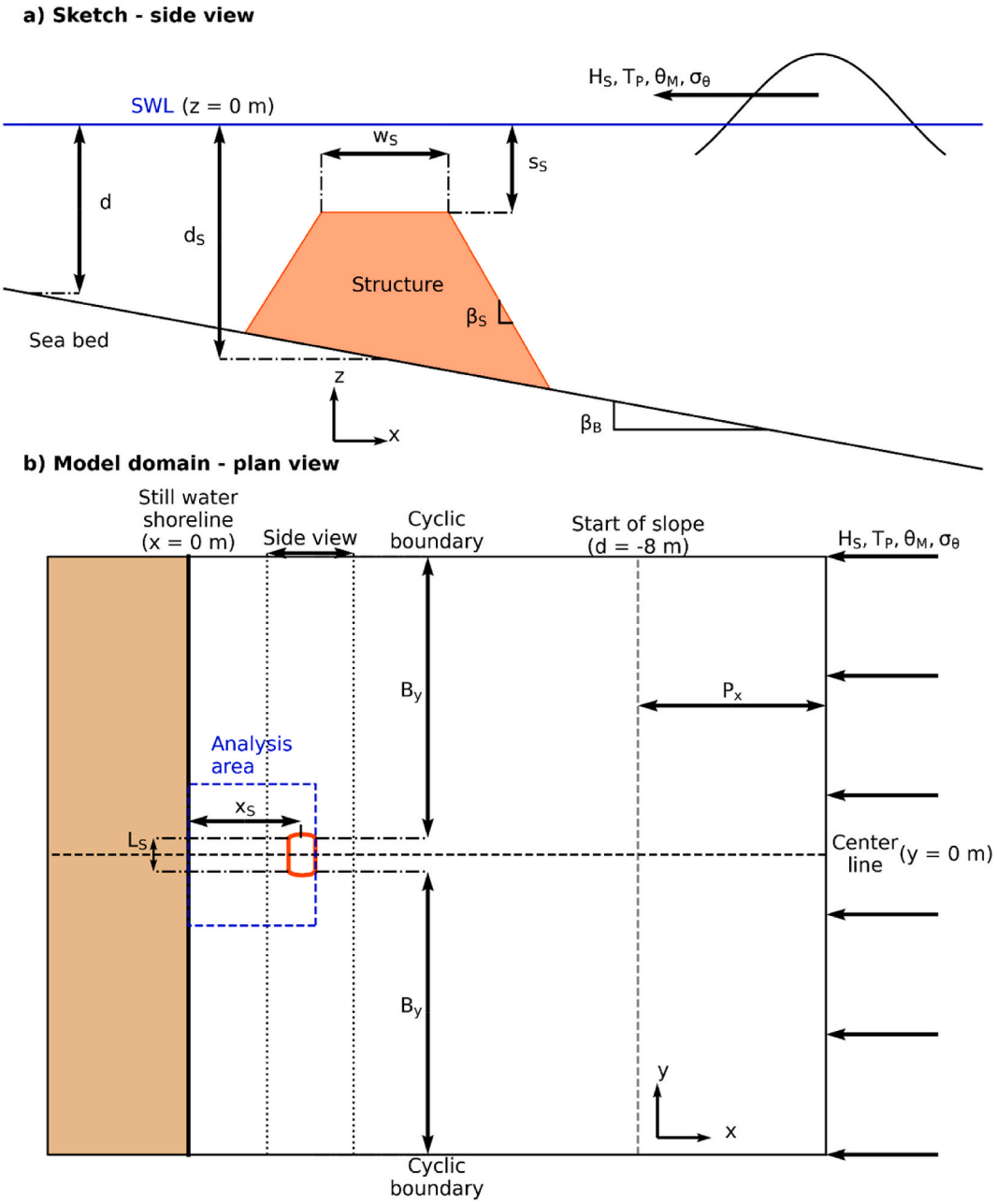

Fig. 2. Schematic views of submerged structure and model domain. (**a**) Side view. (**b**) Plan view. The orange line gives the position of the submerged structure.

nonhydrostatic models (e.g., XBeach NH) to analyse the alongshore variability of runup in field sites with rapidly varying bathymetries (de Beer et al., 2021; Guimarães et al., 2015; Nicolae Lerma et al., 2017; Quataert et al., 2020).

2.2. Parameter space

We used a range of structure geometries that span typically constructed submerged breakwaters (e.g., Ranasinghe and Turner, 2006) that were subjected to a variety of wave conditions. A schematic summarising the layout of the structures, geometric parameters, and notation are provided in Fig. 2 (see Table 1 for a list of all variables), with the focus on variations to four structure parameters (Table 2), namely:

- the distance from the structure crest centre to the shoreline x_S ($100 \leq x_S \leq 250$ m; the subscript $_S$ refers to the submerged structure), which also determines the structure depth d_S for a linear beach profile;
- the (still water) crest level s_S ($-2 \leq s_S \leq 5.0$ m, note that negative values correspond to submerged structures relative to the still water level); for completeness, we also modelled fully emergent structures with a s_S of 5 m that had no wave transmission (i.e., waves did not overtop the structure);
- the alongshore structure length L_S ($100 \leq L_S \leq 400$ m); and
- the cross-shore structure width w_S ($5 \leq w_S \leq 20$ m).

The simulations also considered the following range of irregular wave conditions (Table 2):

- offshore significant wave heights $H_{S,0}$ from 0.5 to 3 m;
- peak wave periods T_P from 7 to 15 s;
- incident wave directions ($0 \leq \theta_M \leq 20^\circ$, with θ_M being the clockwise shore-normal mean wave direction from where waves are coming defined at the offshore boundary); and
- short and long-crested waves ($0 \leq \sigma_\theta \leq 20^\circ$, with σ_θ being the one-sided directional spreading).

Across this parameter space, we investigated how the circulation and runup varied in response to wave breaking over a range of cross-shore positions: offshore of the structure (roughly when $H_{S,0}/d_S > 1$), right over the structure (roughly when $H_{S,0}/d_S < 1$ and $H_{S,0}/s_S > 1$) or onshore of the structure (roughly when $H_{S,0}/d_S < 1$ and $H_{S,0}/s_S < 1$). We note that this last case with shoaling non-breaking waves over the structure has not been addressed in previous studies. Overall, we conducted a total of 176 individual simulations.

2.3. Model configuration

We modelled the wave-driven hydrodynamic processes over a single shore parallel submerged breakwater superimposed on an otherwise alongshore uniform bathymetry (see Fig. 2). The offshore wave maker was located in a flat region, which was followed by a sloping bottom with a fixed constant beach slope of 1:50. The submerged structure was located at the (alongshore) centre of the grid. We conducted a domain convergence study to determine the required domain dimensions for minimising boundary effects in the area of analysis (see Appendix A). We defined the area of analysis as the region in the lee of the structure and from $y = 0$ m (centre) to the structure edges, plus/minus half the distance from the structure to the shoreline, $x_S/2$ (Fig. 2b). The cross-shore flat region length P_x and the distance from the structure to the alongshore boundaries B_Y (Fig. 2b) were defined as 2 and 10 peak wavelengths $L_{P,wm}$ (computed with linear wave theory at the wave maker), which resulted in typical domain length and width of 800 and 1900 m, respectively.

The submerged breakwater had a rectangular crest shape (with width w_S and length L_S), and side slopes of 1:5, which is a typical slope of impermeable breakwaters (van der Meer et al., 2005). In plan view, lateral slopes had semi-circle shapes resulting in roundheads.

We imposed weakly-reflective irregular waves with a JONSWAP spectrum including the bound waves (e.g., Rijnsdorp et al., 2015) at the wave maker (with linear wave theory we accounted for wave shoaling from offshore to the wave maker), and for alongshore boundaries used cyclic conditions (i.e., with the wave-flow recirculating from one side to the other). With the increased size of our alongshore domain, the results in the analysis area are representative for a single structure (i.e., we

Table 1
Notation.

Symbol	Definition	Units
A	Dean profile parameter	$m^{1/3}$
B_y	Alongshore domain length (from outward edge of structure to alongshore boundary)	m
c_f	Dimensionless friction coefficient	–
d	Still water depth	m
d_S	Structure depth (at mid crest) (Fig. 2)	m
E	Depth integrated mean energy density	$m^3\ s^{-2}$
E_{MF}	Mean flow depth integrated energy density	$m^3\ s^{-2}$
E_W	Wave depth integrated energy density	$m^3\ s^{-2}$
f_P	Peak frequency	Hz
g	Gravity acceleration	$m\ s^{-2}$
h	Total water depth	m
h_{rev}	Time-averaged depth where Q_y reverses from diverging to converging circulation (Fig. 6)	m
H_S	Total significant wave height	m
$H_{S,0}$	Deep water significant wave height	m
$H_{S,IG}$	Infragravity significant wave height	m
$H_{S,SS}$	Sea-swell significant wave height	m
L_S	Structure alongshore crest length (Fig. 2)	m
$L_{P,wm}$	Peak wavelength at the wave maker	m
n	Manning roughness coefficient	$m^{-1/3}\ s$
NW_{pp}	Post-processing analysis period in number of peak wave periods	–
NW_{su}	Spin-up period in number of peak wave periods	–
P_x	Deep flat region length (from wave maker to start of slope)	m
$Q_{conv,\ div}$	Cross-shore integrated converging/diverging flow in y-direction (Fig. 6)	$m^3\ s^{-1}$
Q_i	Mass-flux	$m^2\ s^{-1}$
$R2$	2% runup	m
S	Swash	m
S'	Local maxima of swash	m
S_B	Proxy for bed load transport rate	$m^3\ s^{-3}$
s_S	Structure crest level (Fig. 2)	m
S_S	Proxy for suspended sediment transport rate	$m^4\ s^{-4}$
T	Wave period	s
T_P	Peak wave period	s
$u_{B,i}$	Bottom-layer horizontal velocity	$m\ s^{-1}$
u_i	Instantaneous horizontal velocity	$m\ s^{-1}$
$\widetilde{u_i}$	Oscillatory horizontal velocity (calculated by subtracting U from u)	$m\ s^{-1}$
$U_{dep,i}$	Instantaneous depth-averaged velocity	$m\ s^{-1}$
U_i	Mass-flux velocity	$m\ s^{-1}$
w	Vertical velocity	$m\ s^{-1}$
w_S	Structure width (Fig. 2)	m
x	Cross-shore position	m
x_i	Horizontal position	m
x_S	Distance from structure crest centre to still water shoreline (Fig. 2)	m
y	Alongshore position	m
z	Vertical position	m
β_B	Sea bed slope (Fig. 2)	–
β_S	Structure slope (Fig. 2)	–
δ	Minimum threshold depth for definition of beach (for runup calculation)	m
Δx_i	Grid size	m
ζ	Water level deviation from d	m
ζ_b	Water level at beach	m
θ_M	Mean wave direction	°
σ_ζ	Water level standard deviation	m
σ_θ	Directional spreading	°
$\tau_{B,i}$	Bottom shear stress normalised by density	$m^2\ s^{-2}$
$\tau_{B,W,i}$	Wave bottom shear stress normalised by density	$m^2\ s^{-2}$

Table 2
Parameter space.

Type	Variable	Notation	Values (reference)	Units
Structure geometry	Crest level	s_S	−2 – 5 (−0.5)	m
	Distance from structure to shoreline[a]	x_S	100–250 (250)	m
	Structure length	L_S	100–400 (200)	m
	Structure width	w_S	5–20 (10)	m
	Structure depth[a]	d_S	2–5 (5)	m
Wave parameter	Offshore significant wave height	$H_{S,0}$	0.5–3 (1)	m
	Peak wave period	T_P	7–15 (10)	s
	Mean wave direction	θ_M	0–20 (0)	°
	Directional spreading	σ_θ	0–20 (10)	°

[a] For the fixed linear beach profile assumed here the dimensions x_S and d_S were perfectly correlated.

ensured that the boundary effects did not reach the centre of the grid, see Appendix A).

We adopted a grid with cross-shore varying sizes from 1.5 m at the wave maker to 1 m at the shoreline. Based on the changing wave conditions the number of cells per wavelength varied from 30 to 90 at the outer edge of the surf zone. The alongshore resolution was 4 m. Our grid convergence study confirmed that these grid sizes appropriately represented the wave-driven flow and shoreline water levels (see Appendix A). We used two vertically equidistant layers for our simulations, with which the wave dispersion can be accurately represented (Zijlema et al., 2011). To represent wave breaking with a limited number of vertical layers, we used the hydrostatic front approximation (Smit et al., 2013), and we confirmed that the onset of breaking with SWASH default tuning coefficients was correctly accounted for by comparing the results of simulations with 2 and 20 layers (Supplementary Fig. 1). We adopted an initial time step of 0.05 s and target Courant number (CFL) of 0.4–0.8, with which SWASH may adjust the time step over the time.

We used the quadratic friction law to model bottom shear stresses, with the dimensionless friction coefficient c_f being computed with Manning-Strickler formulation $c_f = gn^2(d+\zeta)^{-1/3}$, where g is the gravitational acceleration, n is Manning's roughness coefficient, d is the still water depth, and ζ is the water level. We adopted the SWASH default roughness coefficient n of 0.019 s m$^{-1/3}$, which results in values of c_f that are typical for sandy bottoms (Rijnsdorp et al., 2015). For simplicity, we did not account for the effect of the enhanced roughness of the structure relative to the surrounding beach. To model the horizontal turbulent mixing, the eddy viscosity closure model from Smagorinsky (1963) was used.

2.4. Model output analysis

In this study we adopted a simulation length of 500 peak wave periods T_P (~1 h 23 min for a T_P of 10 s), with the 200 first T_P corresponding to the spin-up period before quasi-steady hydrodynamics conditions are reached, and the last 300 T_P being used for analysis, with each variable being output at 20 Hz (200 f_P for a T_PT_P of 10 s, with f_P being the peak frequency). Our sensitivity analysis with a range of simulation lengths confirmed that the spin-up and analysis periods were adequate for reproducing quasi-steady conditions (Appendix A).

We calculated the total significant wave height as

$$H_S = 4\sqrt{\sigma_\zeta^2}, \tag{1}$$

with σ_ζ being the water level standard deviation. We also calculated the infragravity $H_{S,IG}$ and sea-swell $H_{S,SS}$ components of the significant wave heights with a threshold frequency of $f_P/2$ between SS and IG components. To study the mean flow properties, we calculated the mean water level $\langle\zeta\rangle$, where $\langle\rangle$ indicates time averaging over the last 300 peak wave periods after spin-up, and the mean mass-flux velocity U_i,

$$U_i = \left\langle \int_{-d}^{\zeta} u_i \, dz \right\rangle \Big/ (d + \langle\zeta\rangle), \tag{2}$$

where $i = 1,2$, u_i is the horizontal velocity following the Einstein notation and d is the still water depth, as well as the mean depth-averaged velocity $\langle U_{i,dep}\rangle$. We also calculated the mean (total) bottom shear stresses $\langle\tau_{B,i}\rangle$, with the instantaneous friction $\tau_{B,i}$ being given by,

$$\tau_{B,i} = c_f\left(U_{dep}^2 + V_{dep}^2\right)\frac{u_{B,i}}{\sqrt{u_B^2 + v_B^2}}, \tag{3}$$

where $u_{B,i}$ gives the bottom-layer velocity. With the decomposition of the velocities into mean and oscillatory parts,

$$U_{dep,i} = \langle U_{dep,i}\rangle + \widetilde{U_{dep,i}}, \tag{4}$$

$$u_{B,i} = \langle u_{B,i}\rangle + \widetilde{u_{B,i}}, \tag{5}$$

where the $\sim$ notation above the variable indicates oscillatory components, we calculated the wave-contribution to the bottom shear stress $\tau_{B,W,i}$ as (Rijnsdorp et al., 2021; van Rooijen et al., 2020),

$$\tau_{B,W,i} = c_f\left(\widetilde{U_{dep}}^2 + \widetilde{V_{dep}}^2\right)\frac{\widetilde{u_{B,i}}}{\sqrt{\widetilde{u_B}^2 + \widetilde{v_B}^2}}. \tag{6}$$

To examine the total mechanical energy, we calculated the depth-integrated mean potential and kinetic energy density E as,

$$E = 0.5g\langle\zeta^2\rangle + 0.5\left\langle \int_{-d}^{\zeta} u^2 + v^2 + w^2 dz \right\rangle, \tag{7}$$

that is related to the presence of waves. As will be shown in Section 6.2, the calculation of the mechanical energy allows us to consider a range of physical processes that affects runup. We also calculated the mean flow E_{MF} and wave E_W components of the energy density (e.g., Svendsen, 2005, Chapter 4),

$$E_{MF} = 0.5g\langle\zeta\rangle^2 + 0.5\left(U^2 + V^2\right)(d + \langle\zeta\rangle), \tag{8}$$

$$E_W = 0.5g\langle\widetilde{\zeta}^2\rangle + 0.5\left\langle \int_{-d}^{\zeta} \widetilde{u}^2 + \widetilde{v}^2 + w^2 dz \right\rangle, \tag{9}$$

where $\widetilde{\zeta}$ ($\widetilde{\zeta} = \zeta - \langle\zeta\rangle$) and $\widetilde{u_i}$ ($\widetilde{u_i} = u_i - U_i$) are the oscillatory water level and horizontal velocities, respectively, and w is the vertical velocity.

To calculate the wave runup, we first computed the time series of the beach water levels ζ_b (e.g., Fig. 3a), with the beach position being taken at the most seaward grid cell with a total water depth (δ) of 5 cm or more. Note that we confirmed with sensitivity analysis that a δ of 5 cm provided a robust representation of the 2% runup $R2$ (e.g., Holman, 1986, see Appendix A). Next, we calculated the wave setup at the beach as $\langle\zeta_b\rangle$ and the swash S ($S = \zeta_b - \langle\zeta_b\rangle$). By applying a zero-down crossing method on the swash S we obtained the local maxima of the swash S' (i.e., the peaks, see crosses in Fig. 3a). Next, we added S' to the shoreline wave setup $\langle\zeta_b\rangle$ to calculate runup R, and with the 2% exceedance value we obtained the $R2$ (Fig. 3b). The infragravity and sea-swell (Fig. 3c) contributions to the $R2$ were calculated by filtering the S time series (with a cut off of $f_P/2$) and then isolating the sea-swell and infragravity contributions at the time of the $R2$ events from the unfiltered S time series. The sea-swell and infragravity contributions were then averaged across all runup events greater or equal to $R2$. By dividing the setup and sea-swell and infragravity contributions by the average of 2% highest runup $\overline{R2}$, we calculated the normalised individual contributions of

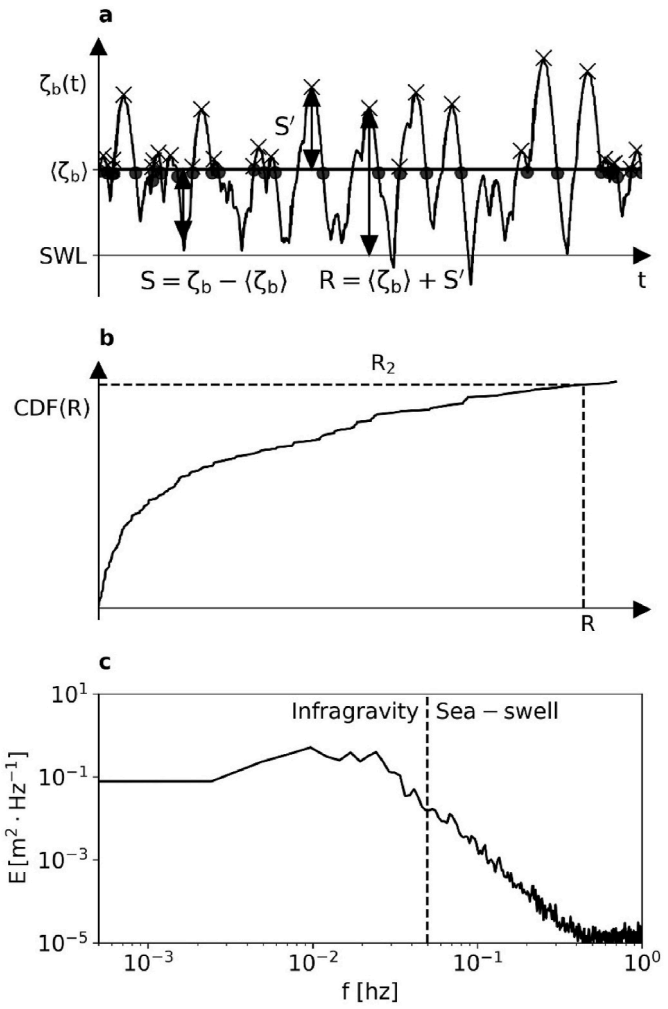

Fig. 3. Demonstration of aspects of runup calculation. (**a**) Time series of water levels at the beach ζ_b, with the circles and crosses representing the location of zero-down crossing points and the runup R (i.e., the peak water levels between zero-down crossings), respectively. Notice that R is the total runup composed of wave setup $\langle\zeta_b\rangle$ and the peaks of the oscillatory (swash) component (S') (note that arrows indicate the respective variables). (**b**) Cumulative distribution function (*CDF*) of runup R, with which the 2% runup $R2$ is calculated. (**c**) Swash spectrum, with the vertical dashed line representing the threshold frequency between the infragravity and sea-swell components of runup ($f_P/2$, with f_P being the peak frequency).

setup $\overline{R2_{\langle\zeta_b\rangle}}$, infragravity $\overline{R2_{IG}}$, and sea-swell $\overline{R2_{SS}}$ components for the $R2$ (e.g., Buckley et al., 2018).

Finally, we used the time-varying bed stress output to calculate proxies for bedload transport rates $S_{B,i}$ and suspended sediment transport rates $S_{S,i}$ (Bagnold, 1963) (see Section 5.2),

$$S_{B,i} = |\tau_B| u_{B,i}, \tag{10}$$

$$S_{S,i} = |\tau_B||u_B| U_{dep,i}. \tag{11}$$

2.5. Model validation

Despite the abundance of 2DV wave flume tests of submerged breakwaters (e.g., van der Meer et al., 2005), few studies have investigated submerged breakwaters in 3D wave basins or the field (and to our knowledge there are no published data sets of detailed velocity or runup observations from a basin or field sites). As a result, there are limited validation datasets for numerical studies of the horizontal 2DH effects of submerged structures. To validate our modelling, we reproduced the physical modelling tests from Ranasinghe et al. (2006), which evaluated the wave-driven flow pattern in the lee of artificial reefs in a wave basin using dye. Their experiments were conducted in a 24.5 m long and 16 m wide wave tank (or in prototype scale, 1225 m long and 800 m wide) with a 12 m long dual piston-type paddle. The bottom profile had a 1:50 sloping bed, and a single artificial reef with isosceles triangle shape (i.e., V-shaped) with side slopes of 1:12 was superimposed on an otherwise alongshore uniform beach (Fig. 4). Here, we considered their tests 'SNCL1-100' and 'SNCL1-250', which simulated a triangle artificial reef with crest submergence level s_S of −0.5 m (all dimensions in prototype scale), length L_S of 100 m, width w_S of 50 m, and with a distance from shoreline to apex of structure crest (or $x_S + w_S/2$ according to our terminology) of 100 and 250 m, respectively. In both tests, shore-normal irregular waves with offshore wave height $H_{S,0} = 1.5$ m and peak wave period $T_P = 10$ s were used. Dye releases around the structure and at the shoreline and a high-resolution digital camera were used to estimate the nearshore flow patterns (Fig. 4).

SWASH was applied to replicate the triangle artificial reefs of their tests 'SNCL1-100' and 'SNCL1-250' with the same setup as described in Section 2.3. The qualitative agreement between SWASH mass-flux velocities and dye tracks (no velocity measurements were made) demonstrates the model capability to reproduce the nearshore flow patterns in the vicinity of submerged structures (Fig. 4). Note that the difference in geometrical shape (i.e., our study considers rectangles, whereas these tests used triangle-shaped reefs) did not result in major changes in the nearshore flow pattern (Section 3.1.1). While the overall lack of physical modelling datasets prevented a detailed quantitative validation, our qualitative comparison of the flow fields demonstrated the ability of our model to reproduce the general aspects of wave-induced circulation in the lee of submerged breakwaters.

3. Nearshore circulation

3.1. Representative features of the nearshore circulation patterns

We first describe the representative flow patterns observed across the parameter space before detailing the response as a function of the structure parameters and wave conditions. Waves propagating over submerged structures drive shoreward mean flows across the structure that diverge in its lee to both sides and then return to the ocean. Fig. 5 captures the variety of flow features that we observed within our parameter space. For all examples in Fig. 5, a single wave condition ($H_{s,0} = 1$ m, $T_P = 10$ s, $\theta_M = 10°$ and $\sigma_\theta = 10°$) and default geometry values ($x_S = 250$ m, $s_S = -0.5$ m, $L_S = 200$ m and $w_S = 10$ m) were used, but with the following parameters then altered: the structure cross-shore position x_S (Fig. 5a and b), structure crest level s_S (Fig. 5c and d) and mean wave direction θ_M (Fig. 5e and f). In Section 3.2 we study how each wave and structure parameter influences the mean flow; however, here these parameters were varied to exemplify certain circulation aspects that are representative of the overall circulation found across our parameter space.

The primary differentiating flow feature is whether converging currents are present adjacent to the shoreline in the lee of the structure. The nearshore hydrodynamics resulting from waves interacting with submerged structures can then be grouped into either: a 2-cell circulation (2CC, e.g., Fig. 5a) or a 4-cell circulation (4CC, e.g., Fig. 5b). The 2CC is characterised by the presence of diverging flow on both sides of the structure, extending from the immediate structure lee all the way to the shoreline (Fig. 5a). The 4CC also features diverging circulation in the direct lee of the structure; however, at some distance farther shoreward (and at the shoreline) the flow converges from both sides. Variations in the wave conditions or structure parameters can cause more complex variations in the specific patterns of the 2CC and 4CC cases. For example, shore-normal waves that do not break over the structure drive a modified version of the 4CC (4CC-NB, where NB stands for non-breaking, Fig. 5c) where the flow convergence occurs at two locations

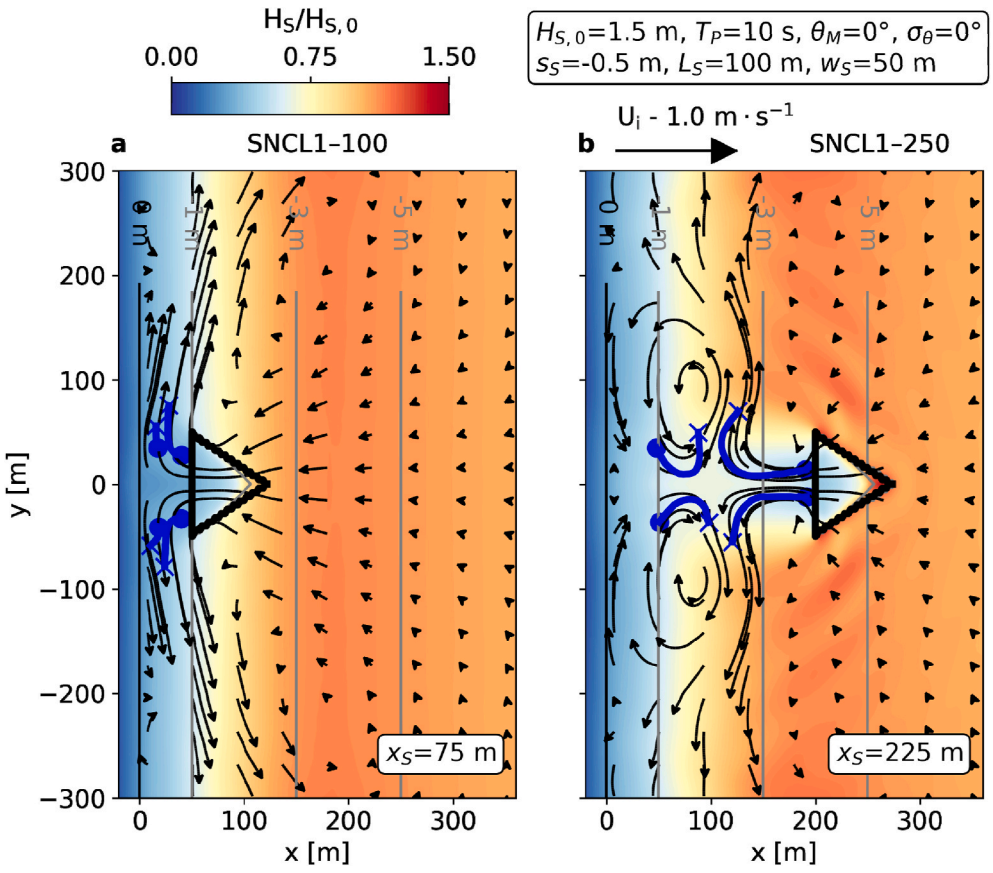

Fig. 4. Map view of normalised significant wave height $H_S/H_{S,0}$ (colours) and mass-flux velocity U (vectors) resulting from waves propagating over triangle submerged structures from Ranasinghe et al. (2006) in prototype scale. **(a)** Structure located 100 m from shoreline (SNCL1-100, see Fig. 5 from Ranasinghe et al. (2006)). **(b)** Structure located 250 m from shoreline (SNCL1-250, see Fig. 6 from Ranasinghe et al. (2006)). The blue lines indicate the dye trajectories (Ranasinghe et al., 2006), with the dots and crosses representing the release point and track, respectively. Structures possess an alongshore length L_S of 100 m, a crest width w_S of 50 m, and a crest level s_S at −0.5 m and are subject to shore-normal waves with significant wave height $H_{S,0}$ of 1.5 m, peak wave period T_P of 10 s, and no directional spreading. Dashed grey lines represent the depth contours and the black line gives the position of the submerged structure.

aligned with the structure edges, rather than in the direct lee/centre of the structure, as is the case when waves break on the structure 4CC-BR (BR stands for breaking over the structure, Fig. 5b). We also identified a specific type of 4CC for emergent structures denoted 4CC-E (E stands for emergent, e.g., Fig. 5d), where the flow strongly converges in the immediate lee of the centre of the structure. Finally, oblique breaking waves result in modified versions of the two-cell circulation (2CC-O, with O standing for oblique e.g., Fig. 5e) and 4-cell circulation (4CC-O, e.g., Fig. 5f), which are characterised by an alongshore shift in the pattern for the shore-normal cases. Note that some slight asymmetries in the wave-driven flows and wave height are observed in all simulations (similar to Rijnsdorp et al., 2020), including those forced by shore-normal incident waves (e.g., Fig. 5a–d). These asymmetries result from transient flow dynamics (e.g., eddies) that initially develop and can persist over many wave periods, which tend to be relatively more important for cases with weaker wave-driven flows (e.g., non-breaking cases, Fig. 5c).

3.1.1. *Shore-normal breaking waves (2CC-BR and 4CC-BR)*

For the 2CC-BR circulation case caused by shore-normal breaking waves (Fig. 5a), waves first shoaled over the lower shoreface and structure slope and then broke over the structure crest. Residual wave energy transmitted past the structure was subsequently dissipated near the shoreline. The shoaling and breaking of waves resulted in setdown over the crest and setup in its lee that progressively increased until the shoreline (not shown). A strong onshore flow developed over the structure which diverged towards the upper/lower sides in the lee of the structure (Fig. 5a).

For the 4CC-BR generated by shore-normal breaking waves (Fig. 5b), waves rapidly shoaled over the structure slope and broke over its crest. The transmitted waves re-shoaled ($70 < x < 200$ m) and broke for a second time closer to the shoreline ($x < 70$ m). The shoaling and breaking of waves over the structure resulted in setdown over the structure crest and setup in the immediate lee ($150 < x < 200$ m) (not shown), which progressively increased at the second breaking zone near the shoreline ($x < 70$ m). A strong onshore flow occurred over the structure that diverged towards the upper/lower sides in its immediate lee. Adjacent to the shoreline ($x < 100$ m), however, the flow converged from both sides ($-250 < y < 250$ m) to the structure centre ($y = 0$ m).

3.1.2. *Shore-normal non-breaking waves (4CC-NB)*

For the 4CC-NB case caused by shore-normal non-breaking waves (Fig. 5c), waves rapidly shoaled over the seaward structure slope, deshoaled over the shoreward slope, and then re-shoaled ($100 < x < 200$ m) and eventually broke near the shoreline ($x < 100$ m). The shoaling and deshoaling of waves over the structure resulted in mild setdown and setup over the crest and in the immediate lee, respectively (not shown). Farther onshore, the setup progressively increased where waves break ($x < 100$ m) and sharply increased at the shoreline (not shown). A moderate onshore flow occurred over the structure that diverged away in its immediate lee. Near the shoreline ($x = 100$ m) the flow converged at two locations approximately aligned with the structure edges ($y = +/-150$ m).

3.1.3. *Oblique breaking waves (2CC-O and 4CC-O)*

The cases with oblique waves interacting with the submerged structure (Fig. 5e and f) were similar to the shore-normal cases. Oblique waves propagating over alongshore uniform beaches drive background alongshore currents along beaches (Longuet-Higgins, 1970). The presence of the structure disrupts this background flow, resulting in an alongshore shift of the flow convergence/divergence (Fig. 5e and f). For the 2CC-O, the flow in the lee of the structure asymmetrically diverges, with the diverging currents either enhanced ($y > 0$ m) or reduced ($y < 0$ m) (Fig. 5e). For the 4CC-O case, the diverging currents in the direct lee

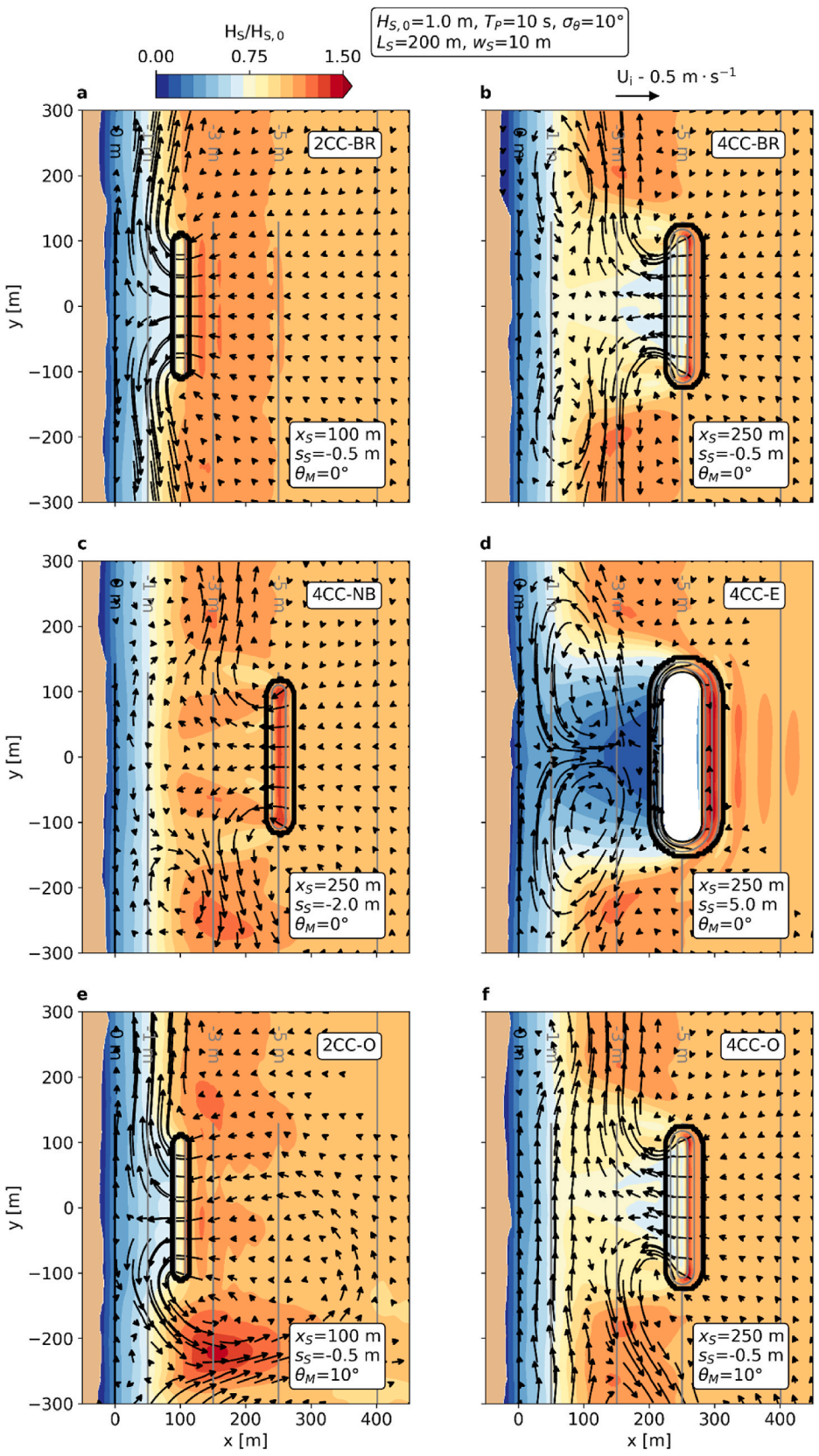

Fig. 5. Map view of normalised significant wave height $H_S/H_{S,0}$ (colours) and mass-flux velocity U (vectors) resulting from waves propagating over a structure. In all panels the structure has a length L_S of 200 m, a crest width w_S of 10 m, and are subject to waves with significant wave height $H_{S,0}$ of 1.0 m, peak wave period T_P of 10 s, and directional spreading σ_θ of 10°. Grey lines represent the depth contours and the black line gives the position of the structure at the bed. 2CC and 4CC represent 2- and 4-cell circulation patterns. 2CC-BR and 4CC-BR result from shore-normal breaking waves over submerged structures, whereas 4CC-NB from shoaling non-breaking waves. 4CC-E results from shore-normal waves interacting with fully emergent structures. 2CC-O/4CC-O correspond to the equivalent of 2CC-BR/4CC-BR for oblique waves.

of the structure were also asymmetrical, but closer to the shoreline ($x <$ 100 m) the flow is dominated by the background alongshore currents, with unidirectional mean flow (Fig. 5f). The alongshore flow thus slows, and even partially reverses, at the shoreline well away from the shoreline at $y \sim$250 m.

3.2. Circulation response to changing wave parameters and structure geometry

Here we use the results from a broader range of cases (Table 2) to investigate how the circulation patterns change with wave parameters and structure geometries. Using the 4CC-BR case in Fig. 5b as a default (reference) case, we investigate how the circulation changes when varying one parameter at a time while holding the other parameters constant. Distinguishing between flow convergence and divergence was relatively straightforward for the illustrative 2CC and 4CC cases in Fig. 5. However, such a distinction can occasionally be more difficult to make for other cases (e.g., cases with weakly converging flows) that required developing a quantitative definition based on the modelled velocity fields. To quantitatively evaluate the circulation response, we established several dimensionless parameters that were used to characterise each flow field. We first calculated the alongshore average of the alongshore mass-flux $\overline{Q_y}^y$ over half of the analysis area (i.e., from $y = 0$ m up to $-x_S/2$ away from the structure edges, shaded area in Fig. 6a and b). Including an alongshore distance equivalent to half the distance between the structure and shoreline ($x_S/2$) beyond the structure edge was required to account for the influence of the structure on the alongshore beyond the structure edges (e.g., note that for the reference case in

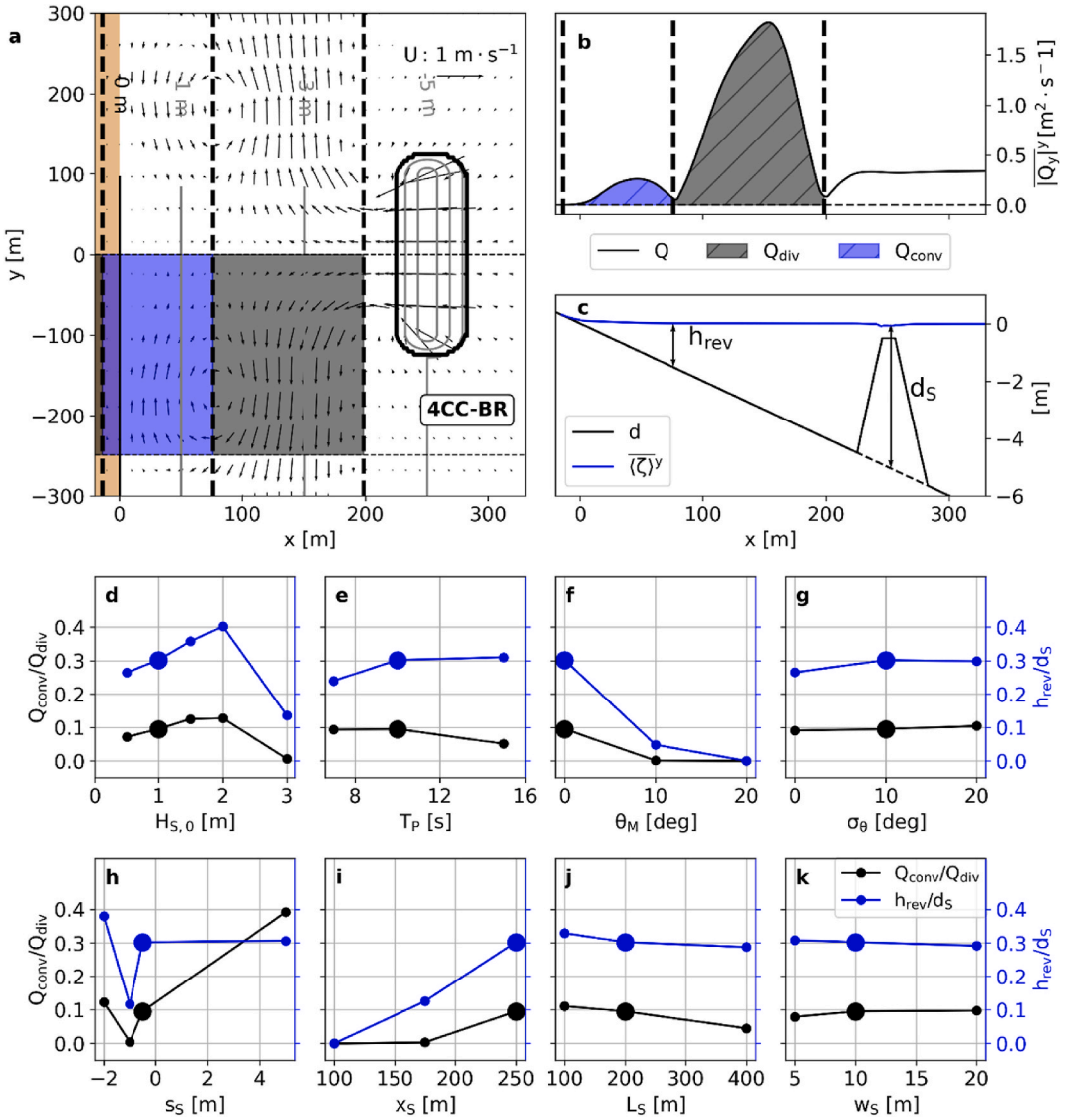

Fig. 6. (**a**) Map view of mass-flux velocity U. (**b**) Cross-shore view of absolute value of mean (over the alongshore) alongshore mass-flux $\overline{Q_y}^y$. (**c**) Cross-shore view of still water depth d and mean (over the alongshore) setup $\langle\overline{\zeta}\rangle^y$. Ratio of converging (e.g., blue hash on **a**,**b**) and diverging (e.g., grey hash on **a**,**b**) cross-shore integrated alongshore mass-flux ratio Q_{conv}/Q_{div} (black on **d**-**k**) and ratio of reversing depth (e.g., h_{rev} on **c**) and structure depth h_{rev}/d_S (blue on **d**-**k**) for varying wave conditions (**d**–**g**) and structure geometries (**h**–**k**). (**d**) Offshore significant wave height $H_{S,0}$. (**e**) Peak wave period T_P. (**f**) Mean wave direction θ_M. (**g**) Directional spreading σ_θ. (**h**) Crest level s_S. (**i**) Distance from structure to shoreline x_S. (**j**) Structure length L_S. (**k**) Crest width w_S. The larger circles indicate the reference simulation (see Fig. 5b and Table 2), which provide the input conditions for every run except for the varying parameter represented on subplots **d**-**k**. $\overline{Q_y}^y$ was calculated by multiplying the alongshore average of the mass-flux velocity V and the mean depth ($d + \langle\zeta\rangle$) over half the analysis area (i.e., from y = 0 m (centre) to the structure edge, minus half the distance from the structure to the shoreline, $x_S/2$ see horizontal dashed lines on **a**), whereas h_{rev} was taken at the location where $\overline{Q_y}^y$ reverses (e.g., see **b**,**c**). Q_{div} and Q_{conv} were calculated with the cross-shore integration of $\overline{Q_y}^y$ over the regions with negative and positive alongshore velocities (see vertical dashed lines on **a**,**b**). Consistent with the definition of converging flows used here (i.e., with opposing alongshore currents, which did not occur for oblique waves), the calculation of Q_{conv}/Q_{div} and h_{rev}/d_S for the wave direction (**f**) considered the side where diverging flow has the same direction as the background alongshore currents (e.g., upper side in Fig. 5e and f).

Fig. 6a converging currents develop at $y = -250$ m, which roughly coincides with the limits of the analysis area). By cross-shore integrating the (absolute) converging Q_{conv} and diverging Q_{div} mass flux within the analysis region separately (blue and grey areas in Fig. 6b) we can compute the ratio Q_{conv}/Q_{div} that provides a normalised measure of the strength of the converging flow. At the cross-shore position where $\overline{Q_y}^y$ changes sign we determined the depth of the reversal, h_{rev}, which was then normalised by the structure depth h_{rev}/d_S (Fig. 6c). This ratio h_{rev}/d_S gives a quantitative measure of the cross-shore extent of the circulation cells.

The circulation ratios Q_{conv}/Q_{div} and h_{rev}/d_S had similar trends for the range of structural and wave parameters considered (Fig. 6d–k, see also Section 3.3), with stronger converging flow (increasing Q_{conv}/Q_{div}) for wider converging cells (increased h_{rev}/d_S). Both ratios varied between 0 and 0.4, indicating that the converging flow was weak compared to the diverging flow for all our simulations. Of all wave parameters, the significant wave height $H_{S,0}$ and the mean wave direction θ_M had the largest influence on the circulation (Fig. 6d,f). Larger wave heights generally resulted in a stronger and wider converging cell; however, a 2CC-BR developed for large wave heights ($H_{S,0} > 2$ m), for which waves began breaking offshore of the structure (note the fixed structure depth d_S of 5 m for these simulations). The peak wave period (Fig. 6e) and the directional spreading (Fig. 6g) did not significantly influence the circulation ratios. As the 4CC-O generated unidirectional currents along the beach due to the wave direction, oblique waves did not drive converging flows thus had null circulation ratios (black in Fig. 6f). Of the structure parameters, the crest level s_S (Fig. 6h) and the distance to shoreline x_S (Fig. 6i) had the largest effect on the circulation. As expected (e.g., Suh and Dalrymple, 1987), emergent structures (i.e., those with positive s_S) consistently resulted in 4-cell circulation patterns (4CC-E, Fig. 6d), with strong and wide converging flows (i.e., large circulation ratios in Fig. 6h). Submerged structures switched between 4CC-BR and 2CC-BR between $s_S = -0.5$ and -1.0 m, resulting from waves breaking over the structure and a 4CC-NB for $s_S =$ - 2.0 m resulting from shoaling non-breaking waves (Section 3.1). Structures located closer to the shoreline had a 2CC-BR pattern (Fig. 6i). The structure length L_S (Fig. 6j) and width w_S (Fig. 6k) did not have a strong influence on the circulation indicators. Overall, the results indicate that $H_{S,0}$, s_S and x_S were the most important parameters that governed the type of circulation pattern (4CC versus 2CC). We also studied how the circulation ratios Q_{conv}/Q_{div} and h_{rev}/d_S responded to wave and structural parameters with a 2CC-BR as a reference case (Fig. 5a), with results (not shown) indicating that only variations of the crest level s_S and distance to shoreline x_S (Fig. 6i) were able to transform the flow either into a 4CC-E (for positive s_S or emergent structures) or 4CC-BR (for large x_S).

3.3. Circulation type classification

Here we propose a set of conditions based on the input wave and structure parameters to predict the circulation resulting from waves propagating over submerged structures. We considered runs where the following parameters were simultaneously varied: $H_{S,0}$ (0.5–1.5 m), T_P (10–15 s), s_S (−1.5 to −0.5 m), x_S (100–250 m), L_S (100–200 m), and w_S (10–20 m), with all cases being forced by shore-normal long-crested waves ($\sigma_\theta = 10°$). We first inspected the circulation ratios Q_{conv}/Q_{div} and h_{rev}/d_S (Section 3.2) to quantitatively classify the flow type into 2CC or 4CC for all simulations (Fig. 7). The simulations reveal two distinct regimes: 1) for limited h_{rev}/d_S ratio values, where Q_{conv}/Q_{div} is near zero and relatively constant over h_{rev}/d_S; and 2) for larger h_{rev}/d_S ratio values where there is a notable upward trend in Q_{conv}/Q_{div} (Fig. 7). Based on these different trends, we classified the flow pattern of runs as 2CC for $h_{rev}/d_S < 0.2$ and 4CC for $h_{rev}/d_S > 0.2$ (note the green vertical dashed line separating the 2CC and 4CC cases in Fig. 7). While a 2CC may present localised areas of convergence at the shoreline, the strength and extension of the converging flow would be restricted due to their limited Q_{conv}/Q_{div} and h_{rev}/d_S ratios. Next, we classified the relationship based on the wave and structure parameters that determine the circulation type: 2CC-BR, 4CC-BR or 4CC-NB. The 4CC-BR cases (red circles in Fig. 7) require the occurrence of wave breaking over the submerged structures, which occurred when $H_{S,0}/|s_S| \geq 1$, combined with wave and structure parameters simultaneously satisfying $|s_S|/d_S \leq 0.12$ and $H_{S,0}/d_S \leq 0.5$; namely, structures with sufficiently large structure depths compared to the crest level, and for cases in which waves do not initiate breaking offshore of the structure. The 4CC-NB cases (blue circles in Fig. 7) require that most waves shoal but do not break over the submerged structures, which is represented by $H_{S,0}/|s_S| < 1$. The 2CC-BR (black circles in Fig. 7) occurs for cases with wave breaking over the submerged structures ($H_{S,0}/|s_S| \geq 1$), and with waves and structure parameters that satisfy either $H_{S,0}/d_S > 0.5$ or $|s_S|/d_S > 0.12$; namely, for most cases where waves initiate breaking offshore of the structure or for structures with limited structure depths compared to the crest level. Overall, our set of predictive relations, which are based on physical processes that govern how waves interact with the structures, were able

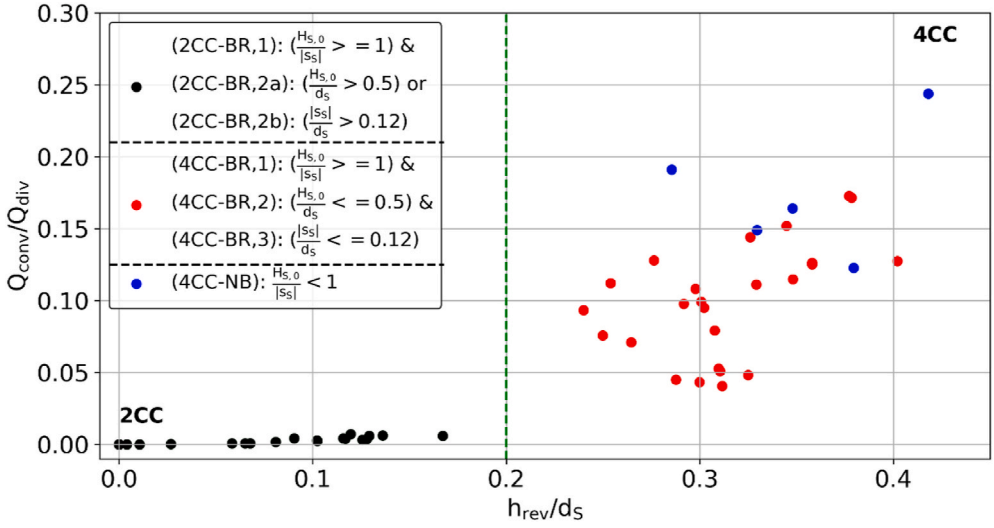

Fig. 7. Ratio of reversing and structure depth h_{rev}/d_S versus ratio of converging and diverging cross-shore integrated alongshore mass-flux Q_{conv}/Q_{div} (for definitions see Fig. 6). The coloured circles represent different input conditions (i.e., wave conditions and structure parameters). The green dashed line denotes our proposed threshold limits ($h_{rev}/d_S = 0.2$) for classifying 2-cell (2CC, $h_{rev}/d_S < 0.2$), and 4-cell (4CC, $h_{rev}/d_S > 0.2$) circulation patterns.

to quantitatively characterise the circulation patterns generated in the lee of the submerged structures.

4. Wave runup

4.1. Representative runup patterns

To determine the influence of submerged structures on shoreline water levels (and thus their ability to offer flood protection), we first assess how wave setup at the shoreline $\langle\zeta_b\rangle$ and 2% runup $R2$ differ with and without the presence of the structures, by initially focusing on the representative cases that resulted in the 2CC-BR and 4CC-BR driven by shore-normal wave breaking (e.g. Fig. 5a and b). Despite the considerable differences in the cross-shore variation of both the sea-swell and infragravity wave heights, both $\langle\zeta_b\rangle$ and R2 were similar for cases with and without the structure (Fig. 8). Onshore of the structure, the infragravity wave heights were mostly similar with values converging at the shoreline (Fig. 8a and b, compare solid and dashed blue lines). For the sea-swell waves, wave breaking on the structure resulted in differences in the wave heights immediately onshore of the structure; however, the wave heights eventually became nearly identical at the shoreline as the sea-swell wave height became depth limited (Fig. 8a and b, dashed and solid black lines).

For both of these representative cases, the largest contribution for the R2 (in both the cases with and without the structure) was wave setup, followed by the sea-swell and infragravity components, respectively (Fig. 8b,d). Although the shoreline water level fluctuations were generally dominated by infragravity components (Fig. 8f), during the extreme events that contributed to the R2, the sea-swell component exceeded the infragravity component. For the 2CC-BR, the presence of the structure resulted in an increase of setup and decrease of the infragravity components of R2 (Fig. 8b). For the 4CC-BR, the presence of the structure did not result in significant changes to the composition of R2 (Fig. 8d).

4.2. Runup response to changing wave parameters and structure geometry

To investigate how setup and runup varied in response to changing wave and structure geometry parameters (Table 2), we followed the same approach as in Section 3.2 where we considered the default 4CC-BR (see Fig. 5b) as the reference case and varied individual parameters while keeping others fixed. The shoreline water level response to the presence of the structure was calculated as the ratio of the 2% runup ($R2_{str}/R2_{no-str}$) and setup ($\langle\zeta_b\rangle_{str}/\langle\zeta_b\rangle_{no-str}$) with and without the structure (Fig. 9b and c). These ratios were alongshore averaged directly in the lee of the structure (black dashed lines in Fig. 9a–c) as well as over the analysis area (solid black lines in Fig. 9a–c). The shoreline water levels ratios $R2_{str}/R2_{no-str}$ and $\langle\zeta_b\rangle_{str}/\langle\zeta_b\rangle_{no-str}$ over the analysis area and in the lee displayed similar trends across the parameter space (Fig. 9d–k). The ratio $R2_{str}/R2_{no-str}$ generally had values close to 1, which indicates that the extreme ($R2$) wave runup was not significantly affected by the presence of submerged structures. Conversely, for fully emergent structures R2 was reduced by 10–40% (Fig. 9h) and decreased approximately linearly for longer structures (red/green lines in Fig. 9j). Wave setup was reduced by 5–20% for all cases, except for the emergent structures, which had reductions of up to 60% (Fig. 9h) and for $x_S = 100$ m (2CC-BR in Fig. 5a), which had an increase of $\langle\zeta_b\rangle$ by 5% (Fig. 9i). Despite the larger percentage reduction in $\langle\zeta_b\rangle$, the absolute reduction was not sufficient to drive large changes in R2 (note that R2 includes $\langle\zeta_b\rangle$, Section 2.4). Overall, the results indicated that impermeable submerged structures only slightly modified the shoreline water levels over this parameter space (see further discussion of the likely reasons in Section 6).

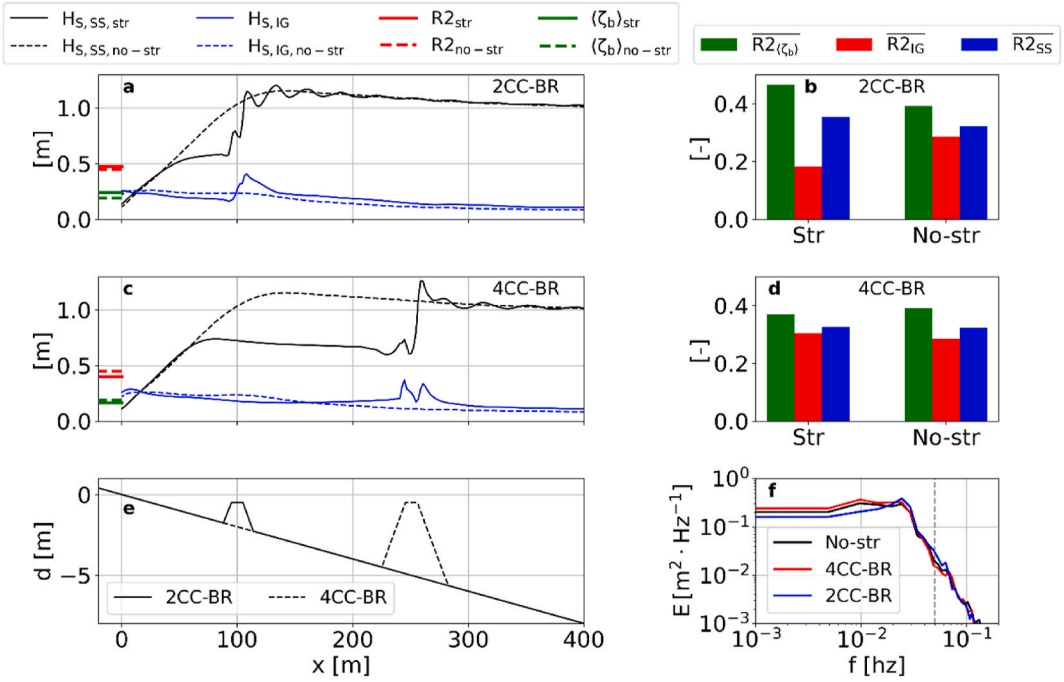

Fig. 8. (**a**,**c**) Cross-shore view of sea-swell ($H_{S,SS}$) and infragravity ($H_{S,IG}$) wave height, 2% runup R2 and shoreline setup $\langle\zeta_b\rangle$. R2 and $\langle\zeta_b\rangle$ are indicated in red and green respectively on the left axis. Structures are located 100 (**a**) and 250 (**c**) m from shoreline. (**b**,**d**) Normalised components of $\overline{R2}$ (average of the 2% highest runup)—setup ($\overline{R2_{\langle\zeta_b\rangle}}$), infragravity ($\overline{R2_{IG}}$) and sea-swell ($\overline{R2_{SS}}$). (**e**) Still water depth. (**f**) Swash spectrum, where the grey vertical line in **f** indicates the threshold frequency between the infragravity and sea-swell components of runup ($f_P/2$, with f_P being the peak frequency). In all panels structures have crest level s_S at −0.5 m and a length L_S of 200 m, a crest width w_S of 10 m and are subject to shore-normal waves with significant wave height $H_{S,0}$ of 1.0 m, peak wave period T_P of 10 s, and directional spreading σ_θ of 10°. All variables were calculated at the alongshore centre position ($y = 0$ m), except for the normalised components of $R2$, which represents the alongshore average over the analysis area (i.e., from $y = 0$ m (centre) to the structure edges, plus/minus half the distance from the structure to the shoreline, $x_S/2$). Cases without the structure (dashed lines in **a**, **c**) were calculated with a run without the structure (i.e., with an alongshore uniform linear profile).

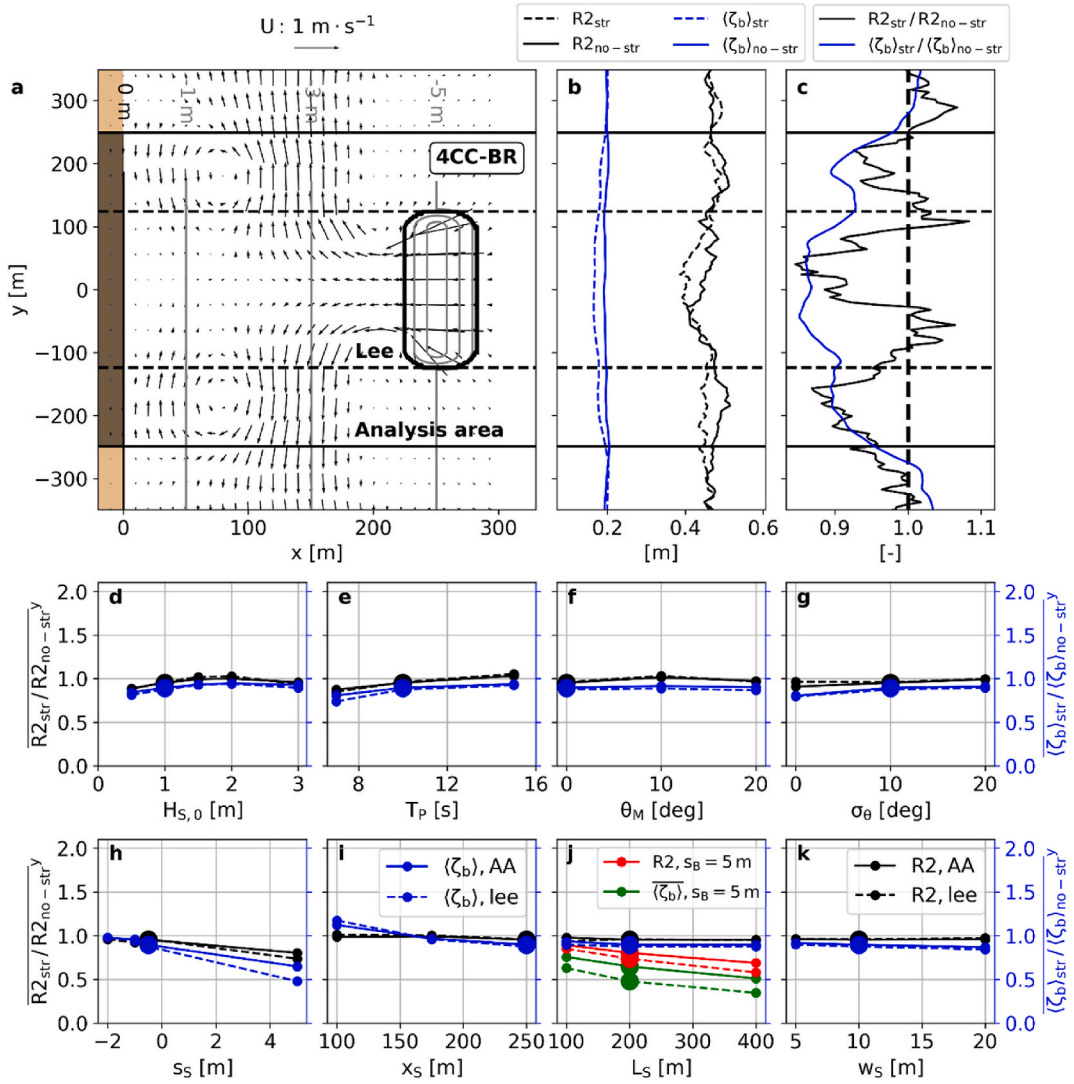

Fig. 9. (**a**) Map view of mass-flux velocity U. (**b**) 2% Runup, $R2$, and shoreline setup, $\langle\zeta_b\rangle$, as a function of alongshore location. (**c**) Ratio of $R2$ and setup with and without the structure $R2_{str}/R2_{no-str}$ and $\langle\zeta\rangle_{bstr}/\langle\zeta\rangle_{bno-str}$. Ratio of mean (over the alongshore in the analysis area [solid line] and directly in the lee [dashed lines]) R2 and $\langle\zeta_b\rangle$ with and without the structure $R2_{str}/R2_{no-str}$ and $\langle\zeta\rangle_{bstr}/\langle\zeta\rangle_{bno-str}$ for varying wave conditions (**d**–**g**) and structure geometries (**h**–**k**). (**d**) Offshore significant wave height $H_{S,0}$. (**e**) Peak wave period T_P. (**f**) Mean wave direction θ_M. (**g**) Directional spreading σ_θ. (**h**) Crest level s_S. (**i**) Distance from structure to shoreline x_S. (**j**) Structure length L_S. (**k**) Crest width w_S. The bigger circles indicate the reference simulation (see Fig. 5b and Table 2), which provides the input conditions for every run except for the varying parameter represented on subplots **d**-**k**. The alongshore average of $R2$ and $\langle\zeta_b\rangle$ was taken over the region in the lee of the structure (black dashed lines on **a**) and in the analysis area (AA) (i.e., the region in the lee of the structure and from $y = 0$ m (centre) to the structure edges, plus/minus half the distance from the structure to the shoreline, $x_S/2$; horizontal black solid lines on **a**). The red/green lines in **j** indicate the runs whose reference simulation had an emergent structure ($s_S = 5$ m).

5. Bed shear stresses and hydrodynamic drivers of sediment transport

The patterns of the wave-driven circulation and wave transformation (including attenuation and changes to nonlinear wave shape) will determine how the structures modify sediment transport and ultimately changes to the shoreline over time. While the focus here is not to directly model sediment transport and morphodynamic changes, which is beyond the scope of the present study, here we use results from the phase-resolved modelling approach to assess intrawave bed shear stresses and velocities, with which we can infer the local hydrodynamic drivers responsible for the spatial patterns of sediment transport. Thus, while we do not attempt to predict quantitative rates of bed load and suspended load, we use the hydrodynamic results to infer how wave and structure parameters alter the spatial distributions of the probable directions of sediment transport.

5.1. Bed shear stresses

We first examined the mean bed shear stresses resulting from waves propagating over the submerged structures by calculating the total ($\langle\tau_{B,i}\rangle$) and wave ($\langle\tau_{B,W,i}\rangle$) shear stress contributions following the approaches outlined in Section 2.4 (see also Rijnsdorp et al., 2021). For both the 2CC-BR (Fig. 10a) and 4CC-BR (Fig. 10d) cases, the total bottom shear stresses generally follow a similar pattern to the mean currents (Fig. 5a and b), with diverging stresses in the structure immediately in the lee of the structure and converging stresses approaching the shoreline only for the 4CC-BR. The total mean bed shear stresses were generally one order of magnitude larger than their wave contribution (notice difference in colours from Fig. 10a,d to Fig. 10b,e), indicating a dominance of the mean flows rather than the nonlinear wave orbital motions to the total stresses. The wave-induced mean bottom shear stresses were dominated by their cross-shore components. At the still water shoreline (x = 0 m), the wave alongshore

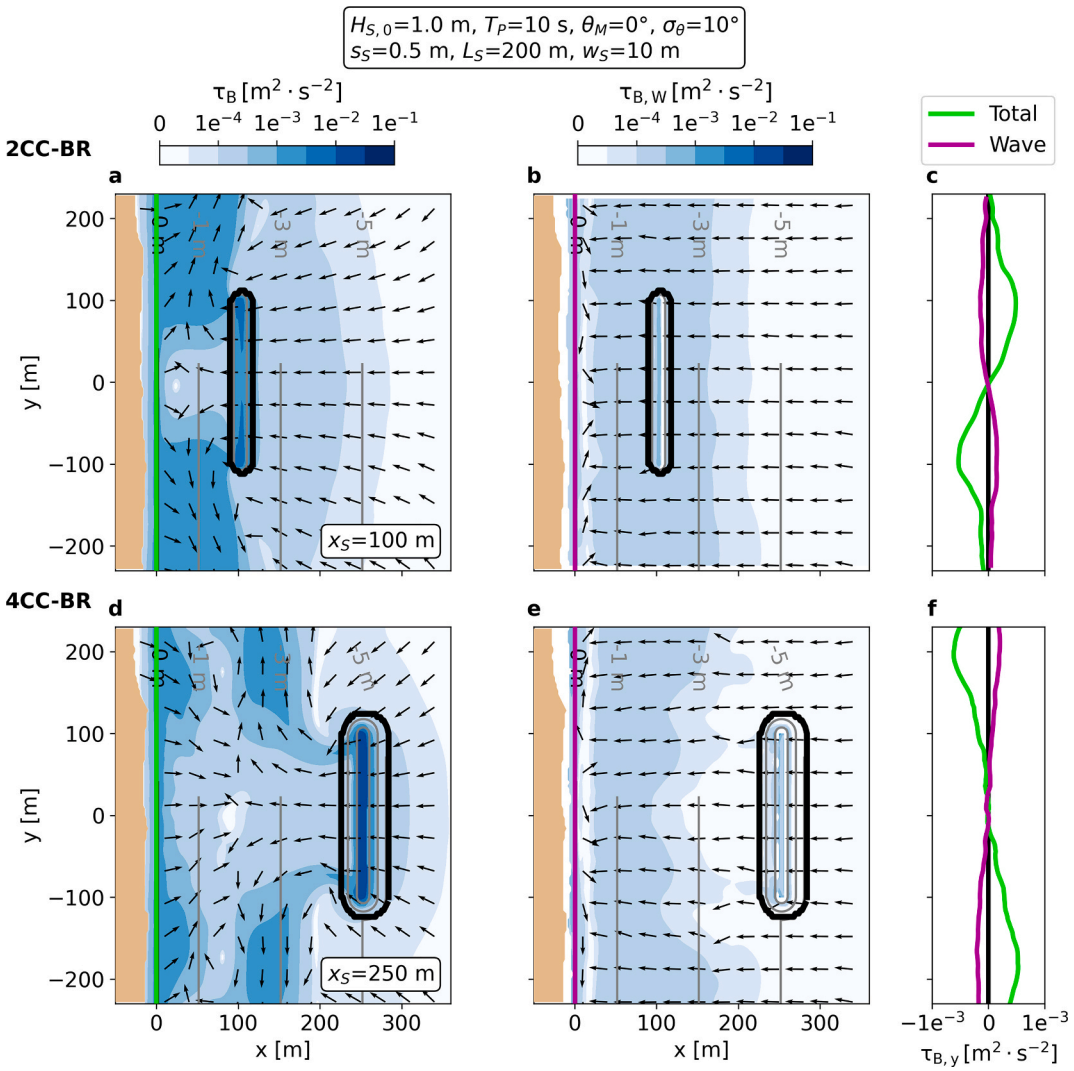

Fig. 10. Map (**a**,**b**,**d**,**e**) view of (**a**,**d**) total τ_B and (**b**,**e**) wave component $\tau_{B,W}$ of the bed shear stresses resulting from waves propagating over a submerged structure. Vectors and colours indicate the direction and magnitude of each value, respectively. (**c**,**f**) Alongshore total (green) and wave component (magenta) of bed shear $\tau_{B,W,y}$ at the still water shoreline (x = 0 m). Structures are located 100 (**a**–**c**) and 250 (**d**–**f**) m from shoreline, with crest level s_S at −0.5 m, and possess a length L_S of 200 m, a crest width w_S of 10 m, and are subject to shore-normal waves with significant wave height $H_{S,0}$ of 1.0 m, peak wave period T_P of 10 s, and directional spreading σ_θ of 10°. Dashed grey lines represent the depth contours and the black line gives the position of the submerged structure at the bed.

bottom shear stresses increased and were about 25% of the total stresses (Fig. 10c,f). Rather than following the 2CC-BR/4CC-BR shoreline divergence/convergence, the alongshore component of the wave bottom shear stresses had opposite values, with converging stresses for 2CC-BR and diverging stresses for 4CC-BR.

5.2. Implications for sediment transport and morphological changes

We examined how the observed flow patterns would likely drive morphological changes by considering two common hydrodynamic proxies for the mean sediment transport: (1) the mean of the product of total (wave and mean flow) bed shear stress and near-bed velocity $\langle|\tau_B|u_{B,i}\rangle$, and (2) the mean of the product of the total shear stress, near-bed velocity and depth-averaged velocity $\langle|\tau_B||u_B|U_{dep,i}\rangle$. These proxies for sediment transport rely on the energetics approach to separately estimate the bedload $S_{B,i}$, Eq. (10), and suspended sediment transport $S_{S,i}$, Eq. (11) (Bagnold, 1963; Bailard, 1981; Roelvink and Stive, 1989). We also calculated the alongshore gradients of the alongshore component of these parameters (see colour contours in Fig. 11) as a proxy for the sign of bed level changes that would be induced by the patterns of sediment transport (i.e., regions of local erosion versus accretion driven by the hydrodynamic patterns, with negative gradients consistent with accretion and positive consistent with erosion). We focus only on the alongshore component of the transport as our primary interest is if the structure likely results in a net increase or decrease in sediment (and thus likely shoreline accretion or erosion, respectively) in the lee of the structure.

We first compared the results for the two representative cases with wave breaking over submerged structures: one with a 2CC-BR (same as Fig. 5a) and one with a 4CC-BR (same as Fig. 5b). Both of the proxies for mean bed load ($\langle S_{B,i}\rangle$, Fig. 11b,e) and suspended load ($\langle S_{S,i}\rangle$, Fig. 11c,f) transport have similar alongshore gradients pattern as the mean flows (Fig. 11a,d), with positive alongshore gradients and potential for shoreline erosion for a 2CC-BR (Fig. 11a–c), and negative gradients and potential for shoreline progradation for cases with a 4CC-BR (Fig. 11d–f). Next, we compared the directions of the mean flow and the two proxies for sediment transports for a 4CC-BR (Fig. 12a and b). The normalised sediment transport and the mean flow vectors generally differ by less than 45°. However, their alongshore component is similar nearly everywhere, and the locations of the 4 circulation cells are approximately the same, indicating that the mean current directions provide robust predictions of the sediment transport patterns. To verify

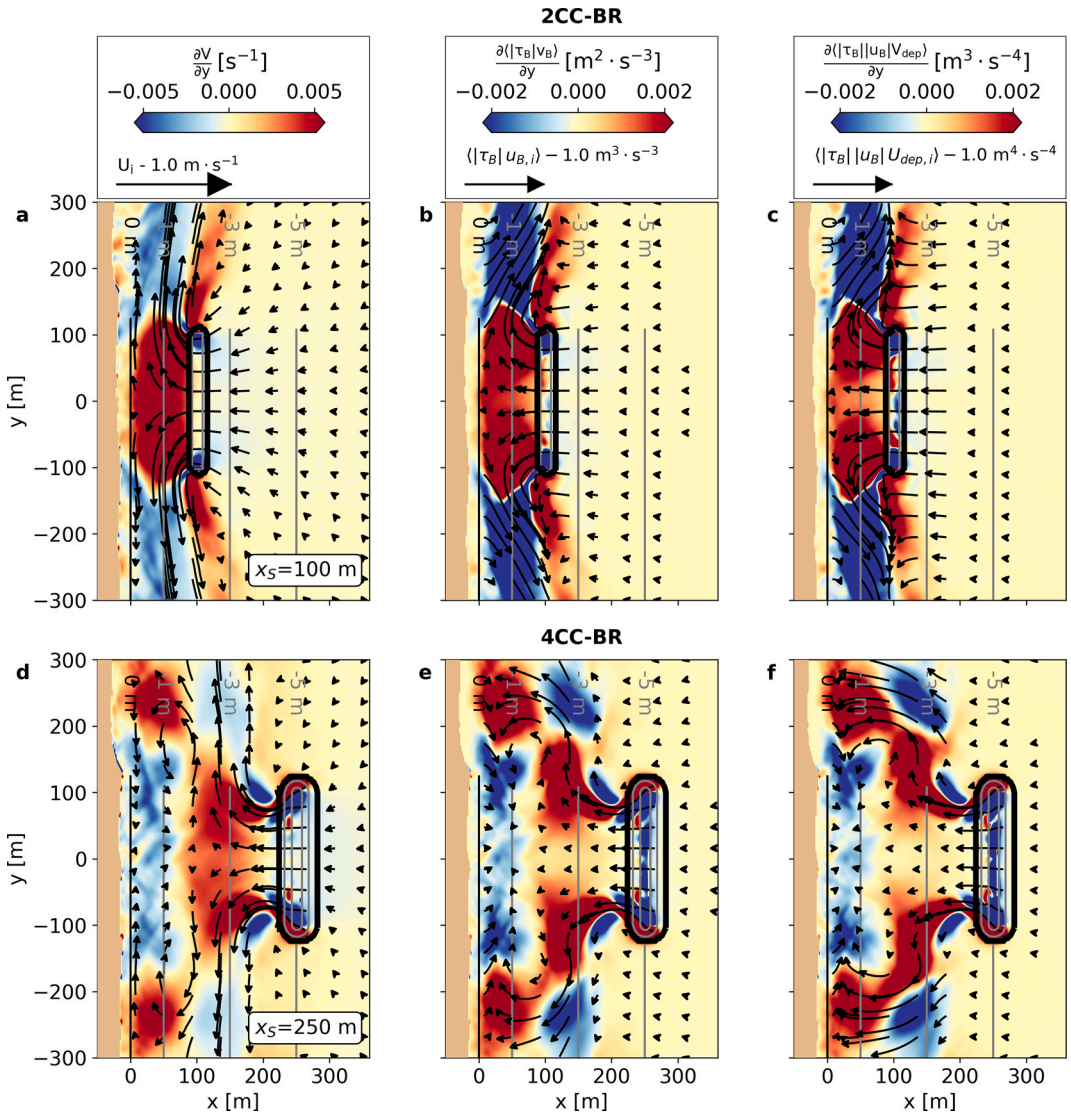

Fig. 11. Map view of predictors for sediment transport—(**a**,**d**) time-averaged mass-flux velocities U_i, (**b**,**e**) product of bed shear stresses and near-bed velocities $\langle|\tau_B|u_{B,i}\rangle$, and (**c**,**f**) product of bed shear stresses, near-bed and depth-averaged velocities $\langle|\tau_B||u_B|U_{dep,i}\rangle$—from waves propagating over a submerged structure. Vectors and colours indicate each variable and its alongshore gradient, respectively. Positive (red) and negative (blue) gradients are likely consistent with erosion and accretion, respectively. Structures are located 100 (**a**–**c**) and 250 (**d**–**f**) m from shoreline, with crest level s_S at −0.5 m and possess a length L_S of 200 m, a crest width w_S of 10 m, and are subject to shore-normal waves with significant wave height $H_{S,0}$ of 1.0 m, peak wave period T_P of 10 s, and directional spreading σ_θ of 10°. Dashed grey lines represent the depth contours, and the black line gives the position of the submerged structure at the bed.

the consistency of these results across our parameter space, we calculated the equivalent to the normalised reversal depth $h_{rev}/\ d_S$ (Section 3.2) using our proxies for $S_{B,i}$ and $S_{S,i}$ estimators for all simulations. Instead of using the alongshore mass-flux (Q_y), we used the proxies for alongshore bedload $\langle|\tau_B|v_B\rangle$ and suspended sediment transport $\langle|\tau_B||u_B|V_{dep}\rangle$, and with those, we calculated the normalised reversal depth for bedload $(h_{rev}/d_S)_{S_B}$ and suspended sediment transport $(h_{rev}/d_S)_{S_S}$, respectively. All three reversing depths are approximately the same (Fig. 12c and d), further reinforcing that the mean currents and sediment transport patterns are primarily aligned indicating that, at least for the parameter space considered, the mean flow directions can be used as a reasonable proxy for sediment transport directions. This is also the case if Fig. 7 is replotted to predict the sediment transport patterns rather than flow structure (based on $(h_{rev}/d_S)_{S_{B,S}}$, not shown). We emphasise that a quantitative evaluation of sediment transport would require a full (intrawave) sediment transport model and is beyond the scope of this study (and not yet implemented in the SWASH model). Yet the overall similarity between the mean flow and the estimated sediment transport directions suggest that the qualitative assessment of the shoreline responses can be made with the mean circulation patterns (see also Section 6.1).

6. Discussion

6.1. Circulation patterns and implications for sediment transport

In this study we applied a nonhydrostatic wave-resolving model to investigate how the mean current fields behind submerged structures respond to structure geometry and incident wave parameters. The type of circulation resulting from shore-normal waves propagating over submerged structures primarily depended on the incident wave height, the crest level, and the structure depth (or distance from the structure to the shoreline). We proposed a set of relations that were able to predict the circulation type as a function of these variables. Our set of predictive relations implicitly inform us (a) whether or not the structures are within the surf zone (i.e., wave breaking or shoaling over the structure),

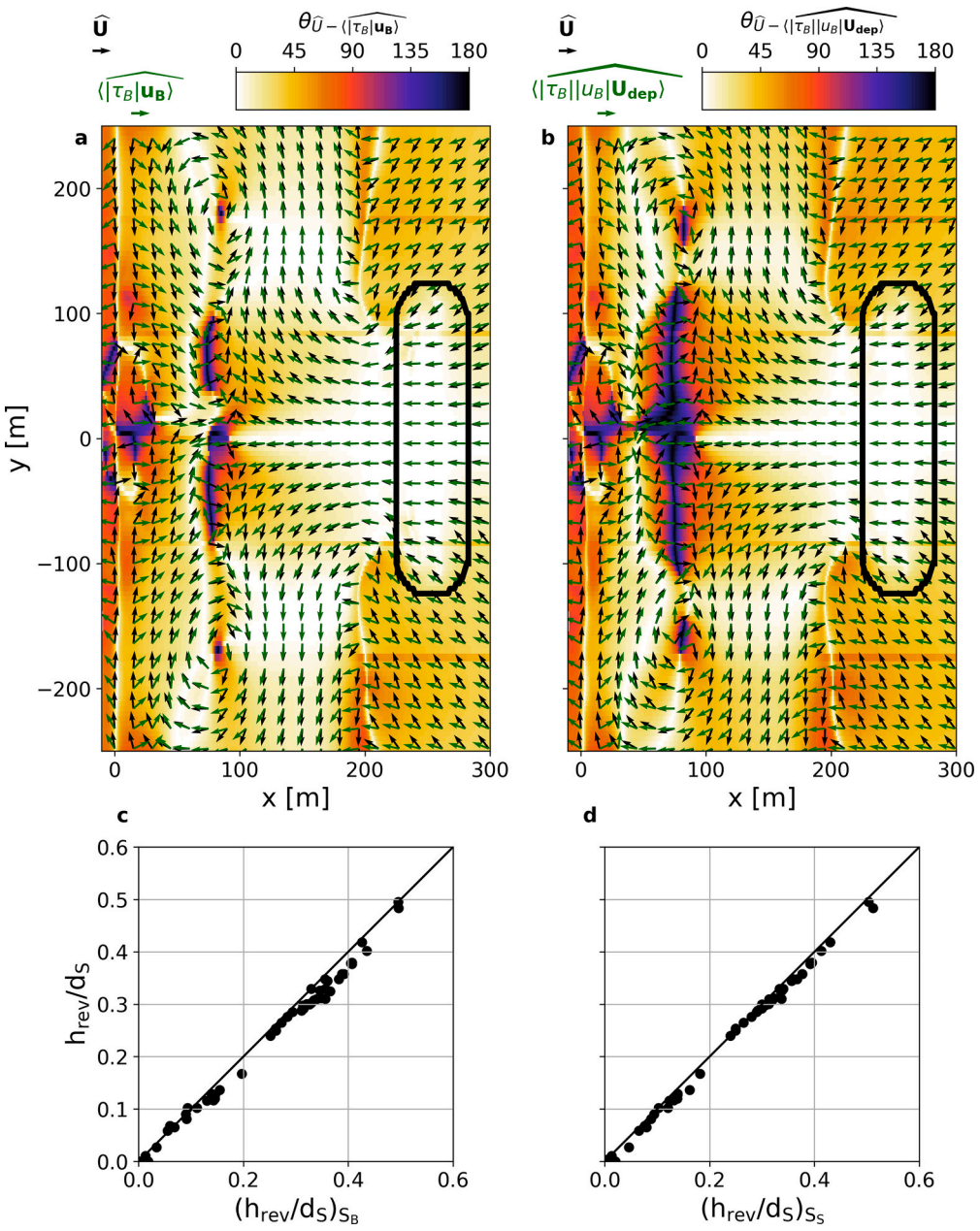

Fig. 12. (**a**,**b**) Map view of normalised mass-flux velocities $\boldsymbol{U}$ (black arrows in **a**, **b**), mean product of bed shear stresses and near-bed velocities $\langle|\tau_B|\boldsymbol{u_B}\rangle$ (green arrows in **a**) and mean product of bed shear stresses, near-bed and depth-averaged velocities $\langle|\tau_B||u_B|\boldsymbol{U_{dep}}\rangle$ (green arrows in **b**)—from waves propagating over a submerged structure. Colours indicate the absolute difference of the angle between $\boldsymbol{U}$ and $\langle|\tau_B|\boldsymbol{u_B}\rangle$ (**a**) and $\boldsymbol{U}$ and $\langle|\tau_B||u_B|\boldsymbol{U_{dep}}\rangle$ (**b**). Structure (black line) is located 250 m from shoreline, with crest level s_S at −0.5 m and has length L_S of 200 m, a crest width w_S of 10 m, and are subject to shore-normal waves with significant wave height $H_{S,0}$ of 1.0 m, peak wave period T_P of 10 s, and directional spreading σ_θ of 10°. (**c**) Ratio of reversing and structure depth h_{rev}/d_S using U versus using $\langle|\tau_B|v_B\rangle$ and (**d**) U versus $\langle|\tau_B||u_B|V_{dep}\rangle$.

(b) if waves initiate breaking offshore of the structure, and (c) the relative distance of the structure to the shoreline.

With these relationships, one can predict the type of wave-driven circulation in the lee of a particular submerged structure for a given sea state. However, real sites may experience substantial temporal variations of wave heights and water levels. As these parameters ultimately control the structure crest level and distance from the structure to the shoreline, real sites may alternate between different types of circulation depending on their temporal variability. Milder waves, which may shoal but not break over the structures, would result in a 4CC-NB, whereas higher waves that will experience depth-limited breaking would yield either a 2CC-BR and or a 4CC-BR. Extreme waves that initiate breaking offshore of the structure would more likely result in a 2CC-BR. Similarly, tidal water level variations could cause oscillations between lower water levels, more likely associated with 2CC-BR or 4CC-BR owing to wave breaking, and higher water levels, more likely associated with 4CC-NB resulting from shoaling non-breaking waves. As the expected types of circulation for a given site depend on its specific met-ocean conditions, site-specific studies will be needed to identify the hydrodynamic response to submerged structures. The oscillation among different classes of circulation will likely influence the shoreline response (see Section 5.2).

The results of our work build on the existing research, particularly the studies from Ranasinghe et al. (2006, 2010) who relied on a coupled wave (phase averaged)-flow model. Ranasinghe et al. (2010) also proposed an empirical model (their Fig. 6) to predict if the flow will be 2CC or 4CC based on the wave and structure parameters. To understand the role of the different modelling approaches (phase-averaged versus phase-resolved) we ran SWASH using their structure parameters, wave conditions and bathymetry which was based on a Dean profile (see Appendix B for details). We found that SWASH predicts similar flow patterns in ~75% of cases (Fig. 13). Understanding the cause of the differences would require a detailed comparison of the respective models and thus is beyond the scope of the present paper. However, the differences in the operating principles of the models utilised (phase-resolved versus phased-averaged) indicate nonlinear processes (e.g.,

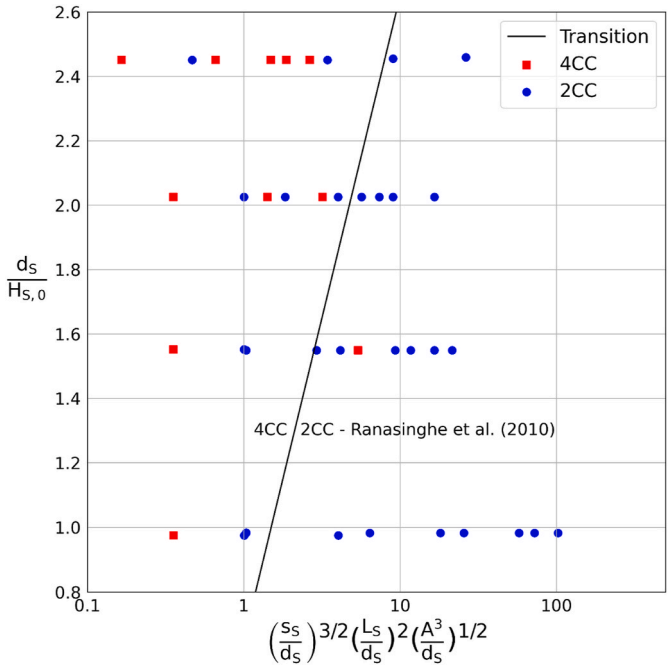

Fig. 13. SWASH results of the simulations of Ranasinghe et al. (2010). In their simulations all points left of the diagonal line were 4CC and all to the right 2CC. The results of the SWASH simulations are indicated by the colours/markers-red squares for 4CC and blue circles for 2CC. For the SWASH simulations, the classification into 4CC and 2CC was based on the ratio of reversing and structure depth h_{rev}/d_S (4CC for $h_{rev}/d_S > 0.2$, and 2CC otherwise; for definitions see Figs. 6 and 7).

energy transfers) are a likely source of these differences.

Although we did not directly simulate sediment transport in this study, the resolved intrawave velocities, water levels, and bottom shear stresses allowed the calculation of proxies for the mean sediment transport, which we can use to infer likely morphological changes. The comparison between the mean currents and sediment transport indicated that they generally follow the same directions, and that the convergence/divergence patterns develop both in the mean flow and sediment transport vectors. With the dominance of the mean currents on the estimated sediment transport patterns, the results suggest that using mean flow patterns close to the shoreline (i.e., converging or diverging flows) can be used as a first indication of the morphological impact of a submerged structure (i.e., shoreline erosion or accretion). While the use of mean current patterns as a proxy for the shoreline response had already been proposed by Ranasinghe et al. (2010), our study quantifies the dominance of the mean currents over the individual and cross contribution of wave orbital motions on sediment transport patterns, thus providing direct evidence that making this approximation is reasonable.

6.2. *Influence of submerged structures on wave runup*

The results obtained over the broad parameter space typical of submerged breakwater applications, indicate that the structures had a limited (~15%) impact on runup. In all simulations we assumed a beach slope of 1/50. To understand if these results were specific to the beach slope considered (and well understood sensitivity of runup on slope) we conducted additional simulations with both a milder (1/100) and steeper (1/20) slope using our two representative cases of a 2CC-BR and 4CC-BR. While the runup changed as a result of the slopes, the changes were mostly consistent across simulations with and without the structure. Accordingly, the normalised 2% runup $R2_{str}/R2_{no-str}$ of these new runs also had values close to 1 (Fig. 14). The similar values for varying slopes suggest that our general findings for the gentle slope of 1/50 are likely consistent over a wider range of beach slopes.

The limited role of the submerged structures in reducing runup is somewhat unexpected given the dissipation of waves on the structure some distance away from the shoreline. To gain additional insight in how the structures impact the waves and the subsequent wave runup in the lee of the structure, we examined the alongshore profile of the depth-integrated mean mechanical energy density, Eq. (7), at several cross-shore locations for our representative case of a 4CC-BR (Fig. 15). We separately considered the wave, Eq. (9), and mean flow portions, Eq. (8), of the energy. The calculation of wave and mean flow energy at several cross-shore locations allows us to characterise physical processes (e.g., dissipation due to breaking, diffraction, and setup development) that

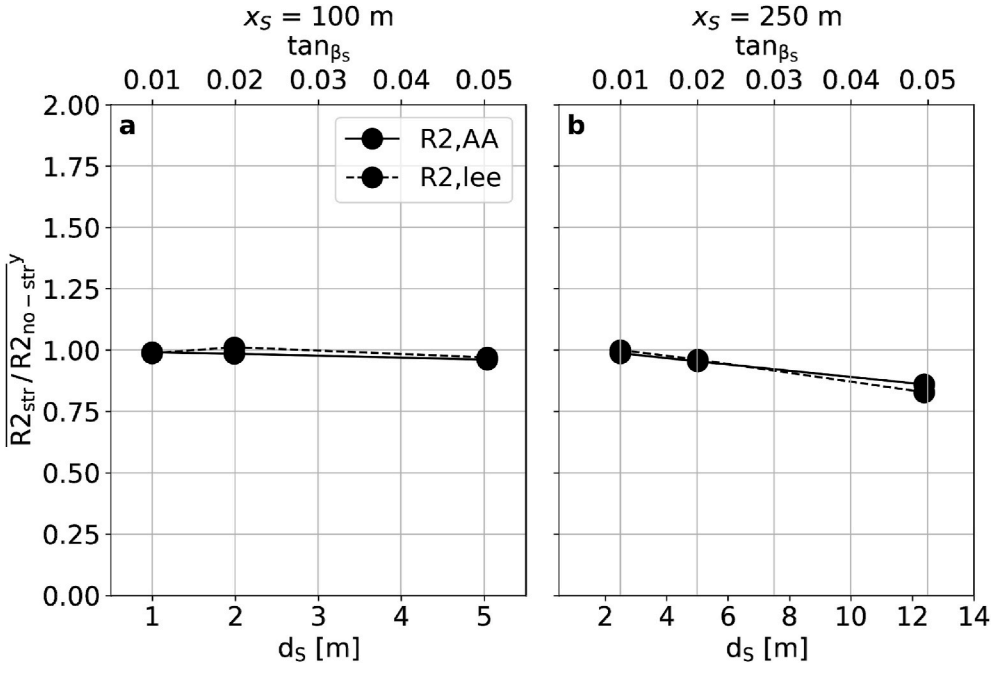

Fig. 14. Ratio of mean (over the alongshore in the analysis area and directly in the lee) 2% runup with and without the structure $R2_{str}/R2_{no-str}$ for varying beach slope (top y-axis) or structure depth (bottom y-axis) while holding a constant distance from structure to shoreline x_S. (**a**) Distance to the shoreline $x_S = 100$ m. (**b**) $x_S = 250$ m. The alongshore average of $R2$ and $\langle\zeta_b\rangle$ was taken over the region in the lee of the structure and in the analysis area (AA) (i.e., the region in the lee of the structure and from $y = 0$ m (centre) to the structure edges, plus/minus half the distance from the structure to the shoreline, $x_S/2$).

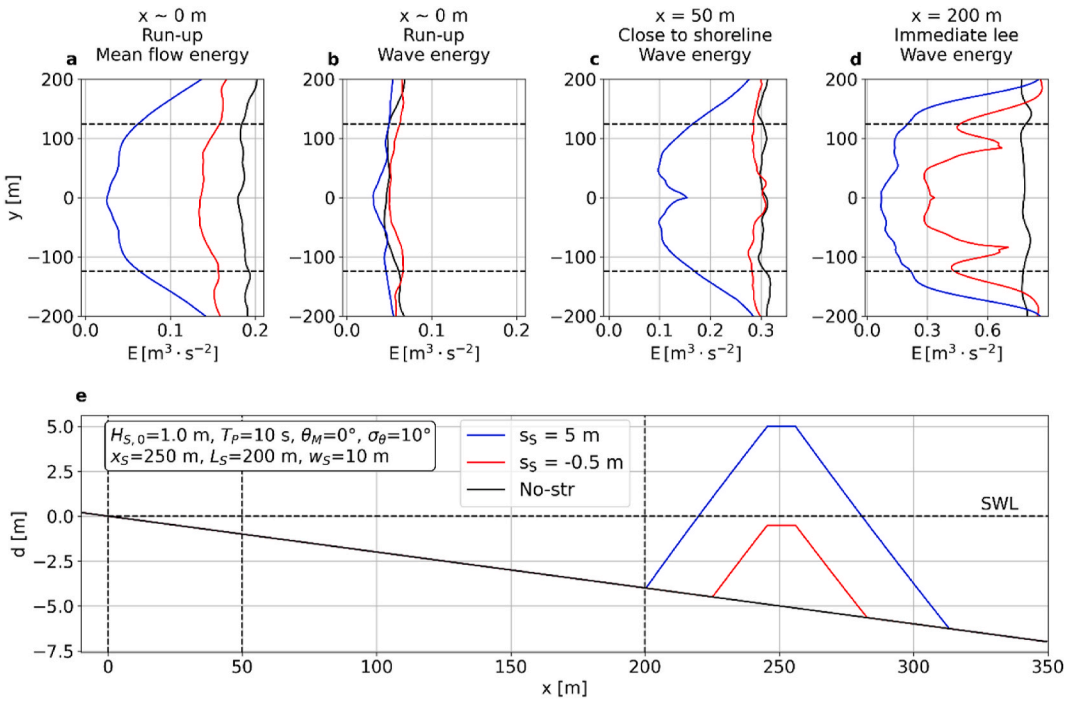

Fig. 15. Alongshore view of the mean-flow (**a**) and wave (**b**–**d**) portions of energy (for definitions see Section 2.4) resulting from waves propagating over structures. The horizontal dashed lines on (**a**–**d**) indicate the alongshore edge of the structures. Cross-shore view of depth profile at the grid centre ($y = 0$ m). The vertical dashed lines on (**e**) indicate the position where the alongshore profiles (**a**–**d**) are taken. Colours indicate the crest level of each run. Structures are located 250 m from shoreline and possess a length L_S of 200 m and a crest width w_S of 10 m; they are subject to shore-normal waves with significant wave height $H_{S,0}$ of 1.0 m, peak wave period T_P of 10 s, and directional spreading σ_θ of 10°.

influence the amount of energy reaching the shoreline, thus controlling runup. In the immediate lee ($x = 200$ m), the dissipation due to breaking results in the reduction of wave energy (Fig. 15d). Close to the shoreline ($x = 50$ m), the wave energy is approximately alongshore uniform (Fig. 15c) owing to wave diffraction and current-induced wave refraction (notice the presence of alongshore converging currents at $x = 50$ m, Fig. 5b). At this cross-shore position, the amount of wave energy is only slightly lower than for the case without the structure, indicating that up to this point the (cross-shore integrated) additional wave dissipation induced by impermeable submerged structures is negligible. At the beach ($x \sim 0$ m), where only potential energy is present, the mean flow energy dominates and is alongshore uniform, and about 10% lower than for the case without the structure (Fig. 15a). Also at the beach, the wave energy is alongshore uniform and approximately the same with and without the structure, but much lower (~70%) than the mean flow energy (Fig. 15b). Overall, the limited additional dissipation over the structure and alongshore transport of wave energy (e.g., diffraction) seem to lead to approximately similar mean energy at the shoreline, which help us explain the limited effect of structures in reducing runup.

As our study considered impermeable smooth structures, we note that it does not account for any effects of porosity or the roughness of specific types of submerged structures, which could influence wave dissipation by the structure. To evaluate the maximum effect that porosities and roughness may impose on shoreline water levels, we considered the wave runup in the lee of emergent impermeable structures, which by not allowing any energy flux (or transmission) are a proxy for fully dissipative structures. With a 5 m emergent structure there is no wave transmission across the structure and thus the shoreline water levels behind the structure strictly depends on the alongshore transport of energy from the region without a structure. To evaluate the role of alongshore transport of energy, we calculated the mean energy density for an emergent structure with s_S of 5 m (blue line on Fig. 15) in a similar fashion as above. In the immediate lee ($x = 200$ m), the wave energy is about 15% of the case without a structure (Fig. 15d), whereas in the inner surf zone ($x = 50$ m), it is about 1/3 of the case without the structure (Fig. 15c). The much-reduced wave energy in the lee of the emergent structure compared to the case with a submerged structure indicates that the alongshore transport of energy (i.e., diffraction and current-induced wave refraction) is less efficient for cases with stronger dissipation/no transmission. Yet the shoreline wave energy is alongshore uniform and about the same as the case without a structure (Fig. 14b). At the shoreline, the mean flow energy is about the same as the wave energy, and about 25% of the mean flow energy for the case without a structure (Fig. 15a and b). Overall, although emergent structures appear unable to influence the shoreline mean wave energy due to the alongshore transport of energy, they cause a considerable reduction in the R2 by affecting the setup at the shoreline $\langle\zeta_b\rangle$ in the lee of the structure.

Finally, we also evaluated the influence of the (emergent) structure length (L_S) in the runup. Short (L_S of 100 m) and long (L_S of 400 m) emergent structures had 10 (30) and 40 (60)% reduction of R2 ($\langle\zeta_b\rangle$) (Fig. 9j, green solid line for the R2 and dashed for $\langle\zeta_b\rangle$), respectively; therefore, the efficiency of the alongshore transport of energy appears inversely proportional to the structure length. These results suggest that the efficacy of highly dissipative structures in reducing the shoreline water levels directly depend on their length. While a detailed study of the shoreline water levels behind porous and fully dissipative structures is beyond the scope of the present paper, our results demonstrate that the wave runup in the lee of submerged structures can be largely influenced by 2D effects; therefore, the wave dissipation (and transmission) induced by them cannot be solely relied upon as a proxy for attenuating shoreline water levels.

7. Conclusions

We studied the wave-induced flow and shoreline water levels in the lee of submerged structures by means of a phase-resolved numerical model. With a wide range of idealised structure geometries and wave

conditions, we found that waves propagating over submerged structures drive a two-cell circulation (2CC)—with diverging flow behind the structure and at the coastline—or a four-cell circulation (4CC)—with diverging currents behind the structure followed by a converging pattern at the shoreline. The qualitative agreement between the mean flow and sediment transport suggests that the mean flow directions can be used as a proxy for sediment transport patterns. By assuming that that bed level changes occur as a result of the alongshore gradient of the mean flow or sediment transport, 2CC and 4CC patterns would thus result in shoreline erosion and accretion, respectively. Within our parameter space, we proposed relationships that were able to predict the circulation type into 2CC and 4CC based on the incoming wave height, crest level and structure depth, or distance to the shoreline.

Our modelling results showed that the submerged structures did not cause significant changes to R2 or $\langle\zeta_b\rangle$, with only up to a 15% reduction of R2 in the structure lee. Despite the much lower wave heights in their lee, the relative increase in the total cross-shore dissipation due to the presence of the structure was found to be limited, which results in roughly similar shoreline water levels with and without the structure. With their minimal effect on the coastal water levels, the main impact of submerged structures on the coastal processes is through modifying the waves propagating over them, which induces current patterns with the potential to cause coastal changes.

While the current work provides an enhanced understanding of the wave driven flow and runup in the lee of submerged structures, it is important to acknowledge that by modelling idealised impermeable smooth structures, our study adopted a simplified representation of submerged structures. We acknowledge that more realistic representations of structures may introduce additional effects to the wave-flow that were not considered in the current study (e.g., porosity and enhanced friction over the structure). Yet our modelling advances our understanding of their general effects on the nearshore circulation and provides the knowledge foundation for further studies that may consider a more extensive range of structure geometries, porosities, and roughness.

Author credit statement

Renan F. da Silva: conceptualization, methodology, software, formal analysis, visualization, writing - original draft, writing - review & editing **Jeff E. Hansen**: conceptualization, writing - original draft, writing - review & editing, supervision, funding acquisition **Dirk P. Rijnsdorp**: conceptualization, writing - original draft, writing - review & editing, supervision **Ryan Lowe**: conceptualization, writing - original draft, writing - review & editing, supervision, funding acquisition **Mark Buckley**: conceptualization, writing - original draft, writing - review & editing.

Declaration of competing interest

The authors declare that they have no known competing financial interests or personal relationships that could have appeared to influence the work reported in this paper.

Acknowledgements

This project forms part of a Ph.D. study by R.F.S. at the University of Western Australia which is supported by the Commonwealth Government through an Australian Government Research Training Program Scholarship. Parts of this research were also supported by the Wave Energy Research Centre through funding provided by the Western Australian Government, via the Department of Primary Industries and Regional Development (DPIRD), and University of Western Australia. Additional support was also provided from the Australian Renewable Energy Agency, Research and Development Programme (grant number 2015RND086) and the Australian Research Council (Discovery Project DP200101545). This work was also supported by resources provided by the Pawsey Supercomputing Centre with funding from the Australian Government and the Government of Western Australia. Any use of trade, firm, or product names is for descriptive purposes only and does not imply endorsement by the U.S. Government.

Appendix C. Supplementary data

Supplementary data to this article can be found online at https://doi.org/10.1016/j.coastaleng.2022.104194.

Appendix A. Sensitivity analysis for model setup

Grid convergence

To determine the optimal grid resolution, we conducted a grid convergence study. We first defined a reference case with the highest resolution ($\Delta x = \Delta y = 1$ m), then we compared the results of a range of grid resolutions ($\Delta x = 1$–2 m, $\Delta y = 1$–4 m) with the reference high resolution case. The comparison included the total significant wave heights H_S, the mean water levels $\langle\zeta\rangle$, the mass-flux velocities U_i and the 2% runup $R2$ (see Section 2.4 for definitions). We calculated the spatial average of the absolute difference between the reference and each simulation inside the analysis area, which encompassed the region in the lee of the structure and from $y = 0$ m (centre) to the structure edges, plus/minus half the distance from the structure to the shoreline, $x_S/2$. All sensitivity simulations had structures with crest level s_S at -0.5 m, distance to shoreline x_S of 250 m, length L_S of 200 m, crest width w_S of 10 m, and were subject to shore-normal waves with significant wave height $H_{S,0}$ of 1.0 m, peak wave period T_P of 10 s, and directional spreading σ_θ of 10°. Both bulk wave and mean flow parameters (i.e., H_S, $\langle\zeta\rangle$ and U_i) had limited variations (close to 5 cm and 5 cm s^{-1}) compared to the reference case across the domain sizes tested (Fig. A1a), which demonstrated the suitability of the grid resolutions Δx of 2 m and Δy of 4 m for the mean flow pattern. However, $R2$ required a finer cross-shore resolution (i.e., with a varying grid size $\Delta x = 1$–2 m, with higher resolution approaching the shoreline) (black vertical dashed lines in Fig. A1a). In our study, we adopted grid resolutions of $\Delta x = 1$–2 m and Δy of 4 m.

Domain convergence

The domain convergence study had a method similar to the grid convergence study, but with varying cross-shore flat region length P_x and the distance from the structure to the alongshore boundaries B_y (Fig. 2). We used reference values for $P_X/L_{P,wm}$ and $B_Y/L_{P,wm}$ (with $L_{P,wm}$ being the peak wavelength at the wave maker) of 4 and 20, respectively, and a range of simulations ($P_X/L_{P,wm} = 1$–4 and $B_Y/L_{P,wm} = 5$–20). Both P_x (Fig. A1b) and B_y (Fig. A1c) had limited deviations (less than 4 cm and 5 cm s^{-1}) from the reference case, and we opted for $P_X/L_{P,wm}$ and $B_Y/L_{P,wm}$ of 2 and 10, respectively.

Spin-up and output

To evaluate the spin-up, we first examined the temporal variability of the domain-integrated kinetic (*KE*) and potential (*PE*) energy and enstrophy (*Z*) (e.g., Feddersen et al., 2011) for a reference simulation (Table 2). Next, we calculated the spatial average of the time derivative of the mass-flux velocities (calculated with time spans of 5 min) inside the analysis area (note that only here we assumed unsteady mass-flux velocities $U(x_i,t)$, with t being the time). After 200 peak wave periods T_P (vertical dashed line in Fig. A2) quasi-steady conditions were observed (i.e., with limited low-frequency oscillation of these three properties, Fig. A2). In addition, sensitivity runs with longer spin-up periods ($NW_{su} = 500$–$1000\ T_P$) confirmed that a spin-up period of 200 T_P was adequate for our study (Fig. A1e). To assess the post-processing period (or analysis period), we conducted sensitivity runs with varying post-processing periods ($NW_{pp} = 150$–$600\ T_P$), and with the results (Fig. A1d) we adopted a post-processing period of 300 T_P (e.g., Fig. A2).

Threshold depth for beach water levels

The calculation of wave setup and runup requires the definition of the position where beach water levels are calculated. Although to date there is no standard depth threshold, δ, for defining the beach position, runup statistics have been shown to be sensitive to this parameter (Fiedler et al., 2020; Stockdon et al., 2006). We conducted sensitivity simulations to verify the effect of varying δ ($\delta = 1$–15 cm) on the *R*2. *R*2 linearly decreased with δ (Fig. A1f), and as the difference between each simulation and the reference case was approximately equal to difference in δ, the results indicate a limited role of the threshold depth δ on the R2 pattern. We decided on a threshold depth δ of 5 cm.

Appendix B. Model setup for Ranasinghe et al. (2010) cases

Ranasinghe et al. (2010) simulated the wave-driven flow in the lee of the submerged structures using phase-averaged numerical modelling. To resolve the phase-averaged circulation they coupled a (linear) mild slope equation wave model and a flow model based on the nonlinear shallow water equations. Their study found that 2CC occurs for cases with $d_S/H_{S,0} < 2\log_{10}\{(s_S/d_S)^{1.5}(L_S/d_S)^2(A^3/d_S)^{0.5}\} + 0.65$, where A is the profile scale parameter (Dean, 1991), whereas 4CC occurs for $d_S/H_{S,0} > 2\log_{10}\{(s_S/d_S)^{1.5}(L_S/d_S)^2(A^3/d_S)^{0.5}\} + 0.65$ (their Fig. 6). To understand the role of the different modelling approaches (phase-averaged versus phase-resolved), we reproduced the cases shown in their Fig. 6 with SWASH and evaluated the flow pattern.

The model setup was the same as described in Section 2.3, except for the assumption of a Dean beach profile $d = Ax^{2/3}$. For all simulations, shore-normal waves with (one-sided) directional spreading of $\sigma_\theta = 22.5^\circ$ and peak wave periods $T_P = 10$ s were prescribed at the wave maker, and submerged structures were superimposed on an otherwise alongshore uniform bathymetry following Dean profile with A of 0.09 $m^{1/3}$ (consistent with a sediment size D of 0.2 mm). A Dean profile with A of 0.09 $m^{1/3}$ corresponds to an average slope of 1/50 (same as employed in this study) from $x =$ 0–100 m ($d = 0$ to -2 m), and to 1/100 from $x = 0$–800 m ($d = 0$ to -8 m). The structures had a constant width w_S of 5 m and side slopes of 0.2. The offshore significant wave height $H_{S,0}$ ranged from 1 to 4 m. Both the distance to shoreline x_S and the structure length L_S had values of 100–400 m. The flow pattern was classified into 2CC and 4CC using the quantitative criteria shown in Section 3.3, with a 2CC for $h_{rev}/d_S < 0.2$ and 4CC for $h_{rev}/\ d_S > 0.2$.

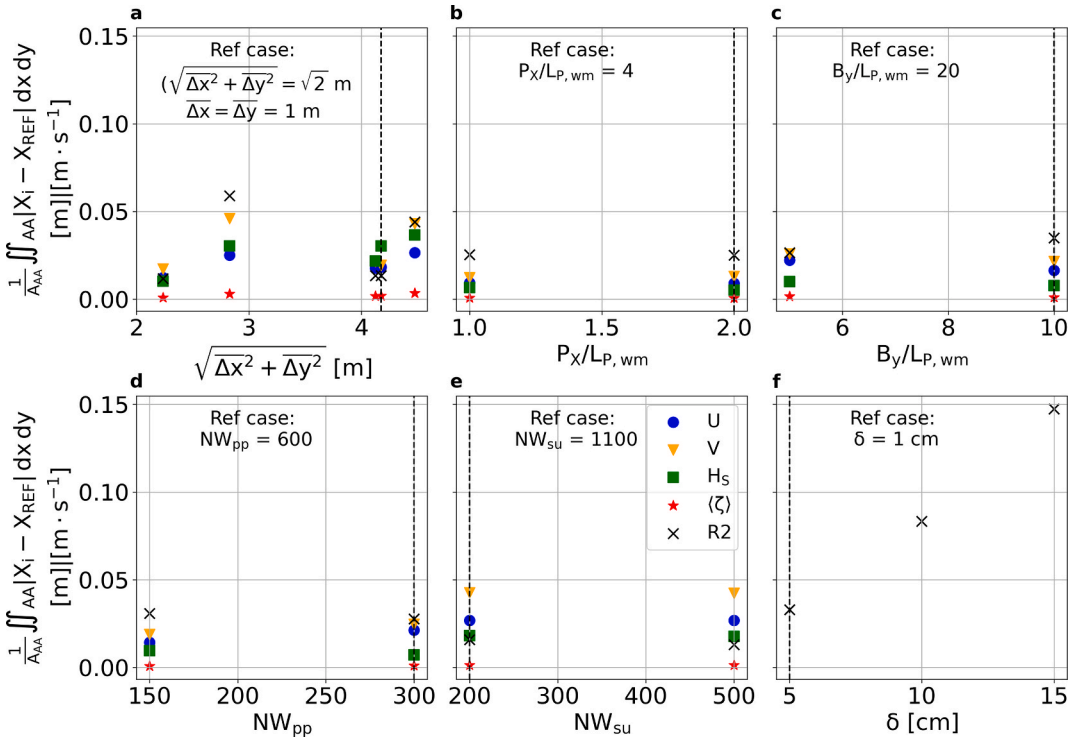

Fig. A.1. Grid averaged absolute difference of bulk parameter—total significant wave height H_S, cross-shore mass-flux velocity U and V, mean water level $\langle\zeta\rangle$ and 2% runup $R2$—between reference case X_{REF} (indicated on top of each subplot) and varying model setup X_iX_i. **(a)** Grid size $\sqrt{\Delta x^2 + \Delta y^2}$. **(b)** Ratio of deep flat region length and peak wavelength at the wave maker $P_x/L_{P,wm}$. **(c)** Ratio of alongshore domain length (from outward edge of structure to alongshore boundary) and peak wavelength at the wave maker $B_y/L_{P,wm.}$ **(d)** Post-processing analysis period in number of peak wave periods (NW_{pp}). **(e)** Spin-up period in number of peak wave periods (NW_{su}). **(f)** Minimum threshold depth for definition of beach position δ (for runup calculation). Grid averaging is calculated in analysis area AA (i.e., region in the lee of the structure and from $y = 0$ m (centre) to the structure edges, plus/minus half the distance from the structure to the shoreline, $x_s/2$). The black vertical dashed line indicates the selected model setup. All simulations had structures located 250 m from shoreline, with crest level s_S at −0.5 m, length L_S of 200 m, crest width w_S of 10 m, and were subject to shore-normal waves with significant wave height $H_{S,0}$ of 1.0 m, peak wave period T_P of 10 s, and directional spreading σ_θ of 10°.

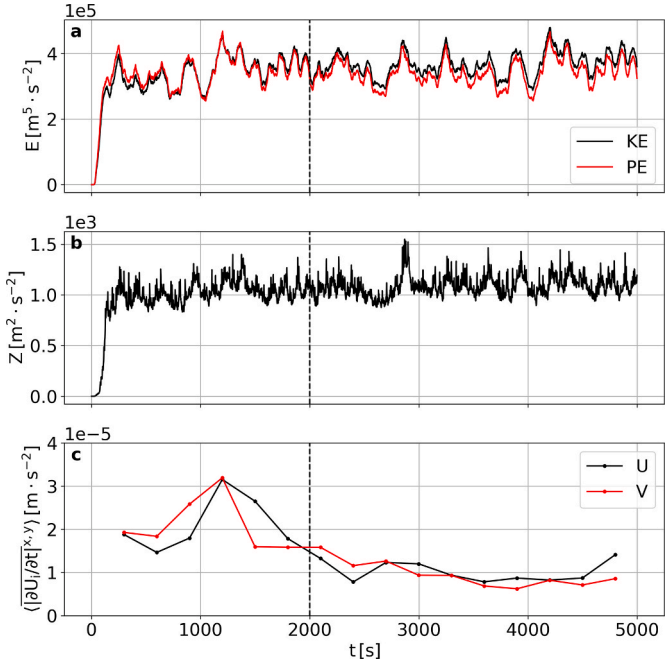

Fig. A.2. Time series of (**a**) domain-integrated kinetic (*KE*) and potential (*PE*) energy, (**b**) domain-integrated enstrophy (Z), and (**c**) spatial average of time-derivative of mass-flux velocities calculated with time spans of 5 min. Structures located 250 m from shoreline, with crest level s_S at −0.5 m, length L_S of 200 m, crest width w_S of 10 m, and subject to shore-normal waves with significant wave height $H_{S,0}$ of 1.0 m, peak wave period T_P of 10 s, and directional spreading σ_θ of 10°. Grid averaging is calculated in analysis area (i.e., region in the lee of the structure and from $y = 0$ m (centre) to the structure edges, plus/minus half the distance from the structure to the shoreline, $x_s/2$).

References

Bagnold, R.A., 1963. Mechanics of marine sedimentation. In: The Sea. Wiley, pp. 507–528.

Bailard, J.A., 1981. An energetics total load sediment transport model for a plane sloping beach. J. Geophys. Res. 86, 10938 https://doi.org/10.1029/JC086iC11p10938.

Black, K., Mead, S., 2001. Design of the gold coast reef for surfing, public amenity and coastal protection: surfing aspects. Source J. Coast. Res. 115–130.

Buckley, M.L., Lowe, R.J., Hansen, J.E., van Dongeren, A.R., Storlazzi, C.D., 2018. Mechanisms of wave-driven water level variability on reef-fringed coastlines. J. Geophys. Res. Ocean. 123, 3811–3831. https://doi.org/10.1029/2018JC013933.

Cuttler, M.V.W., Hansen, J.E., Lowe, R.J., Trotter, J.A., McCulloch, M.T., 2019. Source and supply of sediment to a shoreline salient in a fringing reef environment. Earth Surf. Process. Landforms 44, 552–564. https://doi.org/10.1002/ESP.4516.

d'Angremond, K., Van Der Meer, J.W., De Jong, R.J., 1997. Wave transmission at low-crested structures. In: Proceedings of the Coastal Engineering Conference. ASCE, pp. 2418–2427. https://doi.org/10.1061/9780784402429.187.

da Silva, R.F., Rijnsdorp, D.P., Hansen, J.E., Lowe, R., Buckley, M., Zijlema, M., 2021. An efficient method to calculate depth-integrated, phase-averaged momentum balances in non-hydrostatic models. Ocean Model. 165, 101846 https://doi.org/10.1016/j.ocemod.2021.101846.

de Beer, A.F., McCall, R.T., Long, J.W., Tissier, M.F.S., Reniers, A.J.H.M., 2021. Simulating wave runup on an intermediate–reflective beach using a wave-resolving and a wave-averaged version of XBeach. Coast. Eng. 163, 103788 https://doi.org/10.1016/j.coastaleng.2020.103788.

Dean, R.G., 1991. Equilibrium beach profiles: characteristics and applications. J. Coast Res. 7, 53–84.

Dean, R.G., Chen, R., Browder, A.E., 1997. Full scale monitoring study of a submerged breakwater, Palm Beach, Florida, USA. Coast. Eng. 29, 291–315. https://doi.org/10.1016/S0378-3839(96)00028-2.

Feddersen, F., Clark, D.B., Guza, R.T., 2011. Modeling surf zone tracer plumes: 1. Waves, mean currents, and low-frequency eddies. J. Geophys. Res. Ocean. 116 https://doi.org/10.1029/2011JC007210.

Fiedler, J.W., Young, A.P., Ludka, B.C., O'Reilly, W.C., Henderson, C., Merrifield, M.A., Guza, R.T., 2020. Predicting site-specific storm wave run-up. Nat. Hazards 104, 493–517. https://doi.org/10.1007/s11069-020-04178-3.

Guimarães, P.V., Farina, L., Toldo, E., Diaz-Hernandez, G., Akhmatskaya, E., 2015. Numerical simulation of extreme wave runup during storm events in Tramandaí Beach, Rio Grande do Sul, Brazil. Coast. Eng. 95, 171–180. https://doi.org/10.1016/j.coastaleng.2014.10.008.

Haller, M.C., Dalrymple, R.A., Svendsen, I.A., 2002. Experimental study of nearshore dynamics on a barred beach with rip channels. J. Geophys. Res. 107, 3061. https://doi.org/10.1029/2001JC000955.

Holman, R.A., 1986. Extreme value statistics for wave run-up on a natural beach. Coast. Eng. 9, 527–544. https://doi.org/10.1016/0378-3839(86)90002-5.

Hur, D.S., Lee, W.D., Cho, W.C., 2012. Characteristics of wave run-up height on a sandy beach behind dual-submerged breakwaters. Ocean. Eng. 45, 38–55. https://doi.org/10.1016/j.oceaneng.2012.01.030.

Irtem, E., Seyfioglu, E., Kabdasli, S., 2011. Experimental investigation on the effects of submerged breakwaters on tsunami run-up height. J. Coast Res. 516–520.

Liang, B., Wu, G., Liu, F., Fan, H., Li, H., 2015. Numerical study of wave transmission over double submerged breakwaters using non-hydrostatic wave model. Oceanologia 57, 308–317. https://doi.org/10.1016/j.oceano.2015.07.002.

Longuet-Higgins, M.S., 1970. Longshore currents generated by obliquely incident sea waves: 1. J. Geophys. Res. 75, 6778–6789. https://doi.org/10.1029/JC075I033P06778.

Longuet-Higgins, M.S., Stewart, R.W., 1962. Radiation stress and mass transport in gravity waves, with application to 'surf beats. J. Fluid Mech. 13, 481–504. https://doi.org/10.1017/S0022112062000877.

Lorenzoni, C., Postacchini, M., Mancinelli, A., Brocchini, M., 2012. The morphological response of beaches protected by different breakwater configurations. Coast. Eng. Proc. 1, 52. https://doi.org/10.9753/icce.v33.sediment.52.

Lowe, R.J., Falter, J.L., Monismith, S.G., Atkinson, M.J., Lowe, R.J., Falter, J.L., Monismith, S.G., Atkinson, M.J., 2009. Wave-driven circulation of a coastal reef–lagoon system. J. Phys. Oceanogr. 39, 873–893. https://doi.org/10.1175/2008JPO3958.1.

Marin, T.I., Savov, B., 2017. Verification of the functional efficiency of submerged breakwaters by field measurements. Coast. Eng. Proc. 1, 18. https://doi.org/10.9753/icce.v35.structures.18.

Mohsin, S., Tajima, Y., Sato, S., 2011. Experimental and numerical study on current velocities and vertical profiles of undertow over a submerged breakwater. In: Asian and Pacific Coasts 2011. WORLD SCIENTIFIC, pp. 885–893. https://doi.org/10.1142/9789814366489_0105.

Nicolae Lerma, A., Pedreros, R., Robinet, A., Sénéchal, N., 2017. Simulating wave setup and runup during storm conditions on a complex barred beach. Coast. Eng. 123, 29–41. https://doi.org/10.1016/j.coastaleng.2017.01.011.

Orzech, M.D., Reniers, A.J.H.M., Thornton, E.B., MacMahan, J.H., 2011. Megacusps on rip channel bathymetry: observations and modeling. Coast. Eng. 58, 890–907. https://doi.org/10.1016/J.COASTALENG.2011.05.001.

Pearson, S.G., Storlazzi, C.D., van Dongeren, A.R., Tissier, M.F.S., Reniers, A.J.H.M., 2017. A bayesian-based system to assess wave-driven flooding hazards on coral reef-lined coasts. J. Geophys. Res. Ocean. 122, 10099–10117. https://doi.org/10.1002/2017JC013204.

Pomeroy, A.W.M., Lowe, R.J., Ghisalberti, M., Storlazzi, C., Symonds, G., Roelvink, D., 2017. Sediment transport in the presence of large reef bottom roughness. J. Geophys. Res. Ocean. 122, 1347–1368. https://doi.org/10.1002/2016JC011755.

Quataert, E., Storlazzi, C., van Dongeren, A., McCall, R., 2020. The importance of explicitly modelling sea-swell waves for runup on reef-lined coasts. Coast. Eng. 160, 103704 https://doi.org/10.1016/j.coastaleng.2020.103704.

Quataert, E., Storlazzi, C., van Rooijen, A., Cheriton, O., van Dongeren, A., 2015. The influence of coral reefs and climate change on wave-driven flooding of tropical coastlines. Geophys. Res. Lett. 42, 6407–6415. https://doi.org/10.1002/2015GL064861.

Ranasinghe, R., Larson, M., Savioli, J., 2010. Shoreline response to a single shore-parallel submerged breakwater. Coast. Eng. 57, 1006–1017. https://doi.org/10.1016/j.coastaleng.2010.06.002.

Ranasinghe, R., Turner, I.L., 2006. Shoreline response to submerged structures: a review. Coast. Eng. 53, 65–79. https://doi.org/10.1016/j.coastaleng.2005.08.003.

Ranasinghe, R., Turner, I.L., Symonds, G., 2006. Shoreline response to multi-functional artificial surfing reefs: a numerical and physical modelling study. Coast. Eng. 53, 589–611. https://doi.org/10.1016/j.coastaleng.2005.12.004.

Rathnayaka, D., Tajima, Y., 2020. Applicability of multilayer wave model for prediction of waves and undertow velocity profiles over a submerged breakwater. In: APAC 2019. Springer Singapore, Singapore, pp. 781–788. https://doi.org/10.1007/978-981-15-0291-0_107.

Reguero, B.G., Secaira, F., Toimil, A., Escudero, M., Díaz-Simal, P., Beck, M.W., Silva, R., Storlazzi, C., Losada, I.J., 2019. The risk reduction benefits of the mesoamerican reef in Mexico. Front. Earth Sci. 7, 125. https://doi.org/10.3389/FEART.2019.00125/BIBTEX.

Rijnsdorp, D.P., Buckley, M.L., da Silva, R.F., Cuttler, M.V.W., Hansen, J.E., Lowe, R.J., Green, R.H., Storlazzi, C.D., 2021. A numerical study of wave-driven mean flows and setup dynamics at a coral reef-lagoon system. J. Geophys. Res. Ocean. 126, e2020JC016811 https://doi.org/10.1029/2020JC016811.

Rijnsdorp, D.P., Hansen, J.E., Lowe, R.J., 2020. Understanding coastal impacts by nearshore wave farms using a phase-resolving wave model. Renew. Energy 150, 637–648. https://doi.org/10.1016/j.renene.2019.12.138.

Rijnsdorp, D.P., Ruessink, G., Zijlema, M., 2015. Infragravity-wave dynamics in a barred coastal region, a numerical study. J. Geophys. Res. Ocean. 120, 4068–4089. https://doi.org/10.1002/2014JC010450.

Rijnsdorp, D.P., Smit, P.B., Zijlema, M., Reniers, A.J.H.M., 2017. Efficient non-hydrostatic modelling of 3D wave-induced currents using a subgrid approach. Ocean Model. 116, 118–133. https://doi.org/10.1016/j.ocemod.2017.06.012.

Roelvink, J.A., Stive, M.J.F., 1989. Bar-generating cross-shore flow mechanisms on a beach. J. Geophys. Res. 94, 4785. https://doi.org/10.1029/JC094iC04p04785.

Ryan, S., Algie, C., Macfarlane, G.J., Fleming, A.N., Penesis, I., King, A., 2015. The Bombora wave energy converter : a novel multi-purpose device for electricity , coastal protection and surf breaks. Coast Ports 2015.

Segura, L.E., Hansen, J.E., Lowe, R.J., 2018. Seasonal shoreline variability induced by subtidal water level fluctuations at reef-fringed beaches. J. Geophys. Res. Earth Surf. 1–15. https://doi.org/10.1002/2017JF004385.

Smagorinsky, J., 1963. General circulation experiments with the primitive equations. Mon. Weather Rev. 91, 99–164. https://doi.org/10.1175/1520-0493(1963)091<0099:GCEWTP>2.3.CO;2.

Smit, P., Zijlema, M., Stelling, G., 2013. Depth-induced wave breaking in a non-hydrostatic, near-shore wave model. Coast. Eng. 76, 1–16. https://doi.org/10.1016/j.coastaleng.2013.01.008.

Stockdon, H.F., Holman, R.A., Howd, P.A., Sallenger, A.H., 2006. Empirical parameterization of setup, swash, and runup. Coast. Eng. 53, 573–588. https://doi.org/10.1016/j.coastaleng.2005.12.005.

Suh, K., Dalrymple, R.A., 1987. Offshore breakwaters in laboratory and field. J. Waterw. Port, Coast. Ocean Eng. 113, 105–121. https://doi.org/10.1061/(ASCE)0733-950X(1987)113:2(105).

Svendsen, I.A., 2005. Introduction to Nearshore Hydrodynamics, Advanced Series on Ocean Engineering. WORLD SCIENTIFIC. https://doi.org/10.1142/5740.

Symonds, G., Huntley, D.A., Bowen, A.J., 1982. Two-dimensional surf beat: long wave generation by a time-varying breakpoint. J. Geophys. Res. Ocean. 87, 492–498. https://doi.org/10.1029/JC087IC01P00492.

Traykovski, P., Hay, A.E., Irish, J.D., Lynch, J.F., 1999. Geometry, migration, and evolution of wave orbital ripples at LEO-15. J. Geophys. Res. Ocean. 104, 1505–1524. https://doi.org/10.1029/1998JC900026.

van Der Baan, A.L., 2013. Developing a Design Criterion for the Shoreline Response to Multiple Submerged Breakwaters. MSc thesis. TU Delft.

van der Meer, J.W., Briganti, R., Zanuttigh, B., Wang, B., 2005. Wave transmission and reflection at low-crested structures: design formulae, oblique wave attack and spectral change. Coast. Eng. 52, 915–929. https://doi.org/10.1016/j.coastaleng.2005.09.005.

van Rooijen, A., Lowe, R., Rijnsdorp, D.P., Ghisalberti, M., Jacobsen, N.G., McCall, R., 2020. Wave-driven mean flow dynamics in submerged canopies. J. Geophys. Res. Ocean. 125 https://doi.org/10.1029/2019JC015935, 0–3.

Villani, M., Bosboom, J., Zijlema, M., Stive, M.J., 2012. Circulation patterns and shoreline response induced by submerged breakwaters. Coast. Eng. Proc. 1, 25. https://doi.org/10.9753/icce.v33.structures.25.

Zhang, R., Zijlema, M., Stive, M.J.F., 2018. Laboratory validation of SWASH longshore current modelling. Coast. Eng. 142, 95–105. https://doi.org/10.1016/J.COASTALENG.2018.10.005.

Zijlema, M., Stelling, G., Smit, P., 2011. SWASH: an operational public domain code for simulating wave fields and rapidly varied flows in coastal waters. Coast. Eng. 58, 992–1012. https://doi.org/10.1016/j.coastaleng.2011.05.015.

Zijlema, M., Stelling, G.S., 2008. Efficient computation of surf zone waves using the nonlinear shallow water equations with non-hydrostatic pressure. Coast. Eng. 55, 780–790. https://doi.org/10.1016/j.coastaleng.2008.02.020.

Zijlema, M., Stelling, G.S., 2005. Further experiences with computing non-hydrostatic free-surface flows involving water waves. Int. J. Numer. Methods Fluid. 48, 169–197. https://doi.org/10.1002/fld.821.